Heat transport and flow structures in inclined circular enclosures

Snehal Sunil Patil,[1] V. R. Krishna Priya,[1,2] and Rajaram Lakkaraju[1,*]

[1]*TuRbulent Interfaces And Dispersion (TRIAD) group, Department of Mechanical Engineering, Indian Institute of Technology Kharagpur, West Bengal 721302, India*

[2]*Center for Computational and Data Sciences, Indian Institute of Technology Kharagpur, West Bengal 721302, India*

(Received 4 April 2024; accepted 15 November 2024; published 16 December 2024)

In many thermal convection studies, enclosure inclination against gravity (measured as Φ) changes both flow features and heat transport. We numerically investigated thermal convection in a quasi-two-dimensional circular enclosure in the range $10^7 \leqslant \mathrm{Ra} \leqslant 10^{10}$, $0.1 \leqslant \mathrm{Pr} \leqslant 15$, and $0 \leqslant \Phi \leqslant \pi/2$, where Ra is the Rayleigh number and Pr is the Prandtl number. The dimensionless heat transport follows a nonmonotonic trend due to the change in plume nature near the walls, elimination of secondary rolls, core bulk instabilities, and flow stratification. Our scaling analysis shows dimensionless heat transport is proportional to $(\mathrm{Ra}\cos\Phi)^{1/3}$ at small Φ $(0 \leqslant \Phi < \frac{\pi}{9})$ and to $(\mathrm{Ra}\sin\Phi)^{1/4}$ at large $\Phi(\frac{\pi}{9} \leqslant \Phi \leqslant \frac{\pi}{2})$. In contrast, the Reynolds number based on the global root-mean-square velocity shows a continuous decrease with Φ due to the reduction in buoyancy fluxes, which convert the available potential energy into kinetic energy. Though the buoyancy flux decreases, convection persists through irreversible mixing, which is the dominant mechanism in inclined thermal convection.

DOI: 10.1103/PhysRevFluids.9.124305

I. INTRODUCTION

Thermal convection is ubiquitous in nature [1–6] and in engineering applications [7–13]. The Rayleigh-Bénard (RB) convection serves as a canonical model [14–17], where a fluid layer is heated from the bottom and cooled from the top with an applied temperature gradient collinear to the gravity [18]. Control parameters that govern the RB convection are the Rayleigh number (Ra), which quantifies the buoyancy relative to thermal and viscous effects, and the Prandtl number (Pr), which is the ratio of viscous to the thermal diffusivity [19,20]. In convection-driven thermosiphons [21], solar collectors [21], and heat exchangers [22], a preset inclination (Φ) of the device with the gravity is used to increase the heat transport, though the reasons in the perspective of fluid dynamics are unclear. In the case of planetary flows [21,23] and the polar ice melting [24–27], the external imposed thermal gradient (or solar insolation) may not necessarily be collinear with the gravity and that results in flow features different from the classical RB convection.

The Nusselt number (Nu), which represents the dimensionless heat transport, is one of the key response parameters of thermal convection and demonstrates power-law scaling with Ra, with exponents ranging from 1/4 to 1/3 at inclination angles $\Phi = 0$ [19] and $\Phi = \pi/2$ [28], with anticipated corrections to the scaling exponent with Ra. Though the scaling relations are established for $\Phi = 0$ and $\pi/2$, the behavior of Nu between these two inclination angles is not universal. Earlier research [29–32] indicates that the highest heat transport occurs in inclined convection in between 0 and $\pi/2$. For upright cylinders with low Prandtl number fluids ($\mathrm{Pr} \approx 0.0094$) [29,30],

*Contact author: rajaram.lv@gmail.com

the dependence of $\mathrm{Nu}(\Phi)$ on Φ shows a consistent trend across varying aspect ratio (lateral to vertical dimension Γ) cylinders, i.e., $\mathrm{Nu}(\Phi)$ is minimum at $\Phi = 0$, while the maximum value is approximately reached at $\Phi \approx 0.33\pi$–0.38π. However, the relative heat transport (compared to RB) is significantly influenced by Γ, with a maximum 1100% increase for $\Gamma = 1/20$ and only 21% for $\Gamma = 1$. In the case of small Γ ($= 1/20$) cylinders [29], the dependence of $\mathrm{Nu}(\Phi)$ aligns closely with the dependence of large-scale circulation (LSC) velocity on Φ. However, in the unit aspect ratio cylinder ($\Gamma = 1$) [30], $\mathrm{Nu}(\Phi)$ and LSC velocity do not correlate. The increase in LSC velocity does not necessarily increase $\mathrm{Nu}(\Phi)$ and vice versa, and a simple argument like strengthened LSC corresponds to more plumes and high heat transport may not necessarily be true.

The heat transport dependence on Φ differs for $\mathrm{Pr} < 1$ and $\mathrm{Pr} > 1$. For example, turbulent thermal convection in the upright cylinder ($\Gamma = 1/2$) filled with hot deionized water ($\mathrm{Pr} \approx 2$) showed a two-roll flow structure and considerable reduction in relative heat transport which scales as (1–2Φ) [33]. However, the slight reduction in relative heat transport as $(1 - 0.031\Phi)$ is observed in cylinder ($\Gamma = 1, \mathrm{Pr} \approx 4$) where the flow consists of a single-roll structure [34]. Unlike the $\mathrm{Pr} \ll 1$ case, relative heat transport decreases with a lower aspect ratio. The observed decrement in $\mathrm{Nu}(\Phi)$ is attributed to the development of a two-roll flow structure. These investigations [33,34] were conducted in a narrow region of Φ ($\leqslant 0.04\pi$) and mainly for higher Ra ($\approx 10^{12}$). Numerical simulations for the upright cylinder ($\Gamma = 1$) [32] in the range $10^6 \leqslant \mathrm{Ra} \leqslant 10^8$, $0.1 \leqslant \mathrm{Pr} \leqslant 100$, and $0 \leqslant \Phi \leqslant \pi/2$, report both $\mathrm{Nu}(\Phi)$ and Reynolds number $\mathrm{Re}(\Phi)$ based on time- and volume-averaged root-mean-square velocity, have different maxima and show a nonmonotonic trend in Φ. For $\mathrm{Pr} \leqslant 1$, the maxima for $\mathrm{Nu}(\Phi)$ and $\mathrm{Re}(\Phi)$ are found, respectively, at $\Phi \approx 0.2\pi$ and 0.1π. In contrast, in the case of $\mathrm{Pr} > 1$, they are at $\Phi \approx 0.4\pi$ and 0, indicating the inclination angle alone cannot reveal the observed nonmonotonic trend. The increase in wall shear motions at low Pr (<1) partly explain the observed increase in $\mathrm{Nu}(\Phi)$ and $\mathrm{Re}(\Phi)$, but the same fails to explain high Pr (>1) results [32]. In the case of $\mathrm{Pr} = 4.3$, increased shear generated by the horizontal buoyancy component results in a monotonic increase in Nu with increasing horizontal to vertical buoyancy ratio [35].

The heat transport in rectangular enclosures shows a different trend in Φ compared to upright cylinders. In a rectangular enclosure ($\Gamma = 1, \mathrm{Ra} \approx 10^9, \mathrm{Pr} \approx 6.7$), an increase in Φ gradually changes the LSC from an elliptical to a squarelike shape by eliminating the two counter-rotating corner rolls and shows a monotonic reduction of $\mathrm{Nu}(\Phi)$ with Φ [36]. In the case of high Pr (≈ 480) [37], the flow changes from a soft-turbulent state to a steady laminar state with increasing Φ, and an 85% decay in $\mathrm{Re}(\Phi)$ and a 20% increase in $\mathrm{Nu}(\Phi)$ compared to $\Phi = 0$ are observed. This enhancement in $\mathrm{Nu}(\Phi)$ with Φ is attributed to increased plume coherency. In turbulent RB convection, an increase in shear rate, as well as plume coherency, can enhance heat transport; among these, an increase in plume coherency is more efficient in enhancing heat transport [38]. Inclined rectangular [two-dimensional (2D)] enclosures with large Γ showed multiple flow states and reported $\mathrm{Nu}(\Phi)$ is higher for flow states with more convection rolls [39]. Overall, the mentioned earlier works reasoned variation observed in $\mathrm{Nu}(\Phi)$ can be due to an increase in additional shear [32], existence of multiroll states [39], and flow reversals [40], but the fundamental mechanism behind the nonmonotonicity of $\mathrm{Nu}(\Phi)$ and $\mathrm{Re}(\Phi)$ remained elusive.

In contrast to the mentioned upright cylinders or rectangular enclosures, convection in horizontal cylinders and disks [41–44] is becoming increasingly important due to wide applications such as liquid-cooled sinks [45], falling film around tubes [46], flight cabin ventilation [47], and in process reactor tubes [48]. In the mentioned applications, thermal conditions usually vary around the circumference or periphery of the cylinders, and the scaling laws of heat transport and flow features differ from the classical RB results. For example, convection in a quasi-2D thin circular disk [41] shows periodic emission of massive thermal plumes in the form of coherent oscillations. These intermittent massive plume ejections are created either by boundary-layer instabilities or by spontaneous fluctuations in the core bulk region and are responsible for flow reversals. At high Ra ($\geqslant 10^9$), the flow features usually consist of a single LSC for $\mathrm{Pr} > 4$ and a near-wall jetlike flow for $\mathrm{Pr} < 1$ [49]. At low Ra ($10^7 \leqslant \mathrm{Ra} \leqslant 10^8$) and intermediate Pr ($2 \leqslant \mathrm{Pr} \leqslant 20$), the LSC

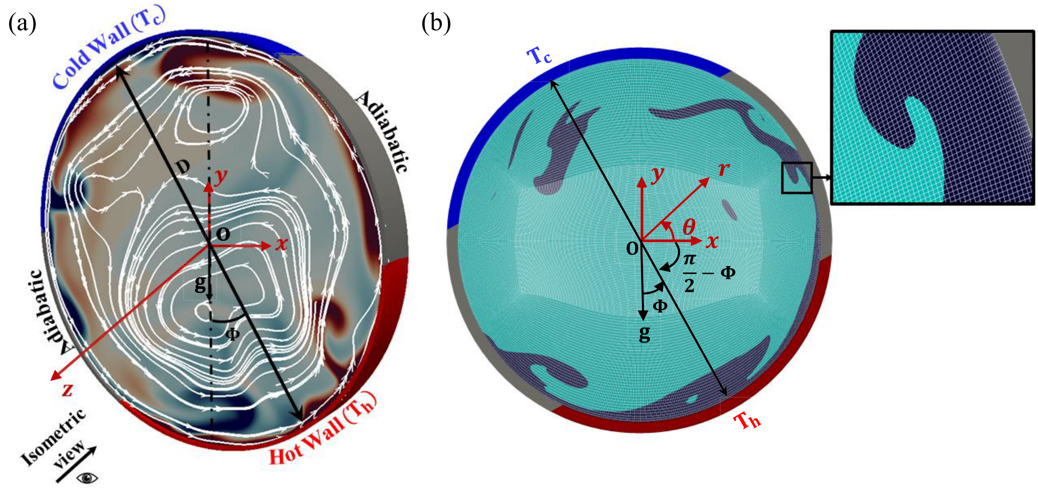

FIG. 1. (a) Schematic of a quasi-2D circular convection as an isometric view. Origin is O, and laboratory frame (x, y, z) axes pass through it. The enclosure is heated to temperature T_h (red), cooled to T_c (blue), and thermally insulated (or adiabatic) on the rest of the circumference. A double arrow line connects the midpoints of conduction walls and makes an angle Φ with gravity $\mathbf{g}$. Instantaneous temperature contours vary linearly from blue (cold) to red (hot), with streamlines in continuous white lines. Simulation for $\mathrm{Ra} = 10^8$, $\mathrm{Pr} = 4.3$, and $\Phi = \pi/6$. (b) A typical computational mesh with a zoom-in of the wall layer with a rising hot thermal plume on the side. Note it is a 2D plane (projection onto the z axis). Polar coordinates are (r, θ).

is accompanied by the secondary rolls (similar to the corner rolls in a square RB), and the flow reversals take place due to the massive plume ejections via a metastable chaotic state [43]. The chaotic state dominates the flow features for $\mathrm{Pr} > 4$ and shows an 8% increase in Nu compared to a stable LSC state. As of now, the role played by the inclination angle to mitigate the formation of secondary rolls and flow reversals in circular disks has yet to be understood at the fundamental level. As a result, the heat transport mechanism and the flow structures are yet to be explored. To address this research gap, we carried out quasi-2D numerical simulations of a circular enclosure heated at the bottom and cooled at the top (see Fig. 1) in the range of $10^7 \leqslant \mathrm{Ra} \leqslant 10^{10}, 0.1 \leqslant \mathrm{Pr} \leqslant 15$ and probed the role played by the inclination angle (Φ) on heat transport and flow features. We varied Φ from zero to $\pi/2$ (in radians) and revealed the route to the energy transfer mechanism by a simplified transient scaling theory and a detailed global energy budget.

Our work is organized as follows: Sec. II for the governing equations and computational methods, Sec. III for flow features, Sec. IV for heat transport and scaling laws, and Sec. V for the global energy budget. In Sec. VI, we have provided a summary and conclusions.

II. GOVERNING EQUATIONS AND COMPUTATIONAL METHOD

In Fig. 1, we have shown an isometric view of a quasi-2D circular enclosure of diameter D, in which the bottom one-third of the circular wall (marked in red) is heated to a temperature T_h, and the top one-third wall (marked in blue) is cooled to T_c. The remaining side portions (marked in gray) of the circular wall are thermally insulated. In a square RB convection, the length of individual hot and cold conduction walls is equivalent to the hydraulic diameter (or four times the area by perimeter); similarly, in circular RB convection, one-third of the circumference is nearly equal (though not precisely) to the hydraulic diameter. A similar conduction wall length ($\pi D/3$) was used in earlier works too [41–43,49].

The conservation of mass, momentum, and the thermal energy equations for an incompressible fluid under the Boussinesq approximation [50–52] are

$$\nabla \cdot \mathbf{u} = 0, \tag{1}$$

$$\frac{\partial \mathbf{u}}{\partial t} + \mathbf{u} \cdot \nabla \mathbf{u} = -\frac{1}{\rho_m}\nabla p + \nu \nabla^2 \mathbf{u} + \mathbf{g}\alpha(T - T_m), \tag{2}$$

$$\frac{\partial T}{\partial t} + \mathbf{u} \cdot \nabla T = \kappa \nabla^2 T, \tag{3}$$

where $\mathbf{u}$ is the velocity field, T is the temperature, p is the dynamic pressure after subtracting the hydrostatic component, and $\mathbf{g}$ is the acceleration due to gravity (and its magnitude is g). The operators $\frac{\partial}{\partial t}$, ∇, and ∇^2 are the time derivative, the spatial derivative, and the Laplacian, respectively. Initially, the fluid inside the enclosure is at rest and maintained at a mean temperature $T_m = (T_h + T_c)/2$. The fluid thermophysical properties such as the density (ρ_m), the kinematic viscosity (ν), the thermal expansion coefficient (α), and the thermal diffusivity (κ) are taken at the fluid mean temperature, T_m. The control parameters are the Rayleigh number, $\mathrm{Ra} = g\alpha(T_h - T_c)D^3/(\nu\kappa)$, and the Prandtl number, $\mathrm{Pr} = \nu/\kappa$. We solved the governing equations (1)–(3) using the second-order Crank-Nicolson scheme to integrate temporal terms, and the Gauss linear schemes for the spatial terms [50]. More details of the numerical schemes used and extensive validation studies are reported in our earlier works [50–52].

A line passing through the midpoints of conduction walls (see Fig. 1) makes an angle Φ with the gravity, which we have considered as the enclosure's inclination angle. We have varied Φ in the range 0–$\pi/2$. In the laboratory frame, the mentioned x and y axes are orthogonal to each other and pass through origin "O," from which the z axis points outward. The gravity ($\mathbf{g}$) acts opposite to the y axis. We have used polar coordinates (r, θ) for heat transport scaling analysis, with standard transforming rules between (x, y) and (r, θ) coordinates. We imposed no-slip boundary conditions on the complete enclosure wall. The disk thickness in the z direction is $D/20$ to confine our work to quasi-2D convection instead of triggering any three-dimensional effects [42,49]. Further, our quasi-2D simulations (compared to three dimensions) help us to probe convection in inclined enclosures over a broad range of Ra-Pr-Φ parameter space, with an excellent boundary-layer resolution. Within limited computational resources, the flow features can be interpreted easily in quasi-2D enclosures, and a direct connection between the flow organization and heat transport is possible.

Figure 1(b) shows the typical computational mesh used in our simulation. The nonuniform structured mesh contains at least 16 grid points near the walls in the radial direction to resolve the boundary layers [39,50,53]. Our computational mesh is designed to capture the wall-bounded motions up to $\mathrm{Ra} = 10^{10}$ (upper limit). Based on grid independence studies and satisfying grid constraints like exact energy balance [54], the same mesh is tested for other Ra, Pr, and Φ. In Table I, details on the spatial and temporal resolutions used in our work are shown, from which we can note that the mesh satisfies the Grötzbach criterion [49,55] to ensure the required resolution. For the temporal resolution, we used a time step increment smaller than 0.007 times the average dissipation timescale [43]. The maximum Courant number in our simulation never exceeded a value of 0.2 to maintain the numerical stability [50]. We have used characteristic scales as the cylinder diameter (D), the free-fall velocity, [$U = \sqrt{g\alpha(T_h - T_c)D}$], and the free-fall time (D/U). The temperature is represented in dimensionless form as $[(T - T_c)/(T_h - T_c)]$. In the following sections $\langle\cdot\rangle$ denotes area average and $\overline{(\cdot)}$ denotes time average.

III. FLOW FEATURES AND REVERSALS

In this section, we describe the influence of inclination on flow organization. Figure 2 shows the instantaneous flow features in a circular RB at a fixed $\mathrm{Pr} = 4.3$, but for a wide range of Ra and Φ (see Movie 1 and Movie 2 from the Supplemental Material [56]). For $\mathrm{Ra} = 10^7$ and $\Phi = 0$, we observed the LSC or primary roll with secondary rolls and occasional flow reversals. With an

TABLE I. Spatial and temporal resolutions used in our simulations at different Ra. The minimum and maximum range of Pr is mentioned. Grid spacing (Δg) and time step increment (Δt) compared with Kolmogorov (η_K) and Batchelor (η_B) scales. The estimation of $\eta_K = (\nu^3/\epsilon)^{1/4}$, $\eta_B = \eta_K \mathrm{Pr}^{-1/2}$, and Kolmogorov timescale $\tau_\eta = (\nu/\epsilon)^{1/2}$ involves the kinetic energy dissipation $\epsilon = \nu^3 D^{-4} \mathrm{Pr}^{-2} \mathrm{Ra} \overline{\langle |\nabla \mathbf{u}|^2 \rangle}$. Here $\langle \cdot \rangle$ denotes the planar average and $\overline{(\cdot)}$ denotes the time average. The last column of the table for time average (after discarding transients of $5000tU/D$) statistics in terms of free-fall time. We have carried out 232 simulations spanning 4 Ra, 5 Pr, and 14 Φ.

Ra	Pr	$\Delta g/\eta_K$	$\Delta g/\eta_B$	$\Delta t/\tau_\eta$	tU/D
10^7	[0.1, 15]	[0.07, 0.005]	[0.02, 0.02]	[0.003, 0.005]	50000
10^8	[0.1, 15]	[0.14, 0.011]	[0.04, 0.04]	[0.004, 0.005]	100000
10^9	[0.1, 15]	[0.29, 0.024]	[0.092, 0.091]	[0.006, 0.007]	100000
10^{10}	[0.1, 15]	[0.42, 0.05]	[0.14, 0.16]	[0.006, 0.006]	100000

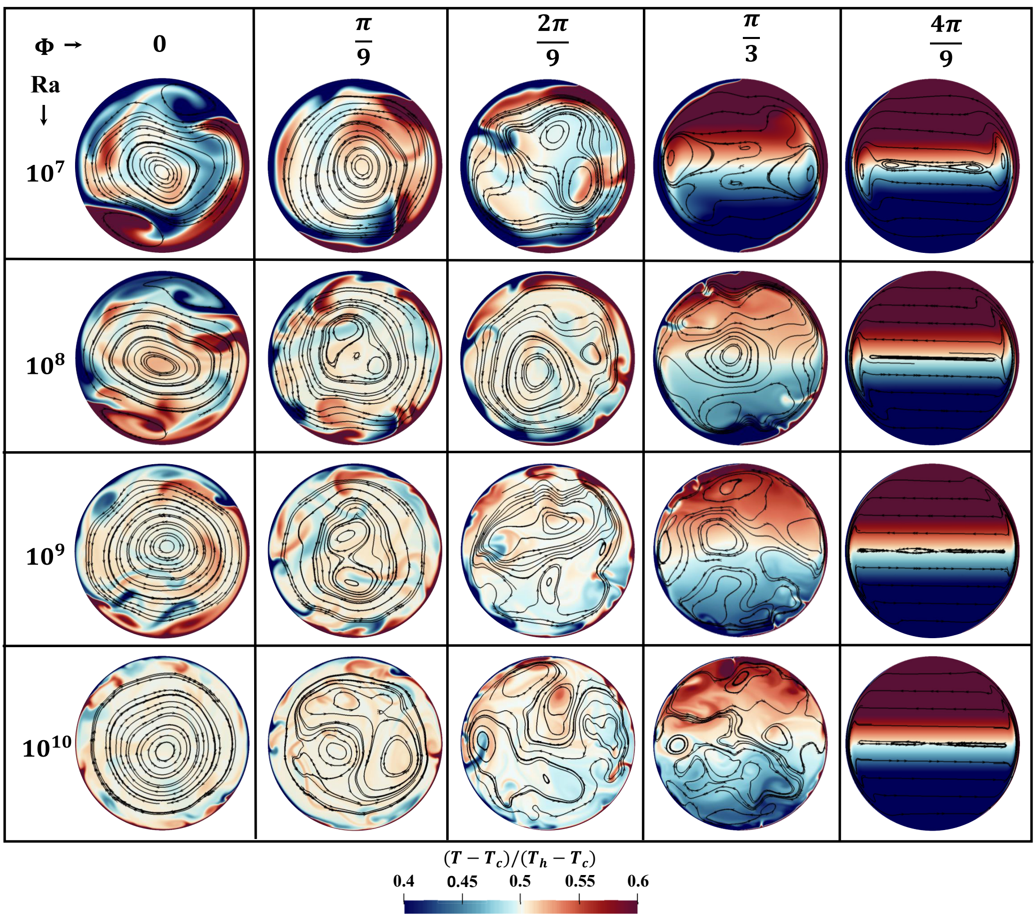

FIG. 2. Instantaneous temperature field (color contours), velocity vectors, and streamlines in a circular enclosure for Pr = 4.3. Colors for temperature vary linearly from 0.4 (blue) to 0.6 (red). Simulations for Ra = 10^7–10^{10} and $0 \leqslant \Phi \leqslant \pi/2$.

increase in Ra ($\geqslant 10^8$), the primary LSC strengthens, and the secondary rolls weaken; thus, no flow reversals (at least up to time $10^5 D/U$). These findings are consistent with Ref. [43]. Beyond Ra $\geqslant 10^9$, the primary LSC occupies almost all the enclosure without any secondary rolls. Our results are consistent with earlier experimental findings by Wang *et al.* [42]. With an increase in Φ, thermal plumes rise or fall along the enclosure wall, and the LSC maintains a nearly circular shape without any secondary rolls and flow reversals. A further increase in Φ leads to the core bulk zone instabilities in the form of a dipole or a tripole mode, which further destabilizes into a multiroll state. Flow stratification occurs for a large inclination angle ($\Phi \geqslant \pi/3$), in which the upper half of the enclosure consists of hot and the lower half of cold zones. In that situation, plumes rarely rise along the walls. At sufficiently high Ra ($\approx 10^{10}$), the bulk core instabilities are triggered even in the stratified zones. Similar flow transitions are observed in a square enclosure [36] filled with water (Pr ≈ 6.3) where an increase in Φ (up to 0.29π) changes the elliptical shape LSC to a square shape by eliminating the secondary rolls, and for $\Phi > 0.29\pi$ flow features become relatively complicated. However, in the case of a square enclosure filled with high Pr (≈ 480) fluid [37], the flow at $\Phi = 0$ shows "soft turbulence" with weak LSC. With an increase in Φ ($\approx 5\pi/36$), the elliptical LSC becomes more prominent and gradually evolves into a square shape at higher angles. Similarly, in the case of cylinders, complicated multiroll flow structures are developed for $\Phi = 0$, and inclination reorganizes the flow to fix the direction of LSC and results in structured flow [31,32].

In Fig. 3, we have shown the flow features for different Pr and Φ at fixed Ra $= 10^7$ (see Movies 3 and 4 from the Supplemental Material [56]). For small Pr ($\leqslant 0.1$), the thermal diffusivity is high, and plumes are confined in near-wall regions without any strong eruption from the wall. We observe a single roll structure up to $\Phi \leqslant 2\pi/9$ (in the diffusion dominant state), and beyond $\Phi \geqslant \pi/3$, the core bulk zone instabilities set in. For high Pr ($\geqslant 7$) and $\Phi = 0$, massive plumes erupt, and a chaotic state with intermittent flow structures such as dipole, tripole, and quadrupole develop. The thermally stratified zones are visible for $\Phi \geqslant \pi/3$ at Pr $\geqslant 1$ but absent at Pr $\leqslant 0.1$. However, results from cylindrical convection cells [32] show stratified zones are visible for both Pr $\ll 1$ and Pr $\gg 1$ after $\Phi \geqslant 0.3\pi$.

To quantify the energy content and the large-scale flow features, we used the Fourier mode decomposition [40,50,57,58]. The instantaneous amplitude of a particular Fourier mode is calculated as

$$A_x^{(m,n)}(t) = \iint 2u(x, y, t)\sin(m\pi x)\cos(n\pi y)dx\,dy, \tag{4}$$

$$A_y^{(m,n)}(t) = \iint -2\,v(x, y, t)\cos(m\pi x)\sin(n\pi y)dx\,dy, \tag{5}$$

where (u, v) are the velocity components in the x and y directions, m is the number of rolls in the x direction, and n is the number of rolls in the y direction. The Fourier mode decomposition was initially designed to study flow behaviors in square domains [40,57,58]. Xu *et al.* [43] extended this approach to a circular enclosure. In their work [43], the Fourier method is applied for the velocity field on a square domain of length equal to the diameter of the circular enclosure around the origin and sets the velocity vectors that fall outside the circular enclosure to be zero; here, we followed the same approach. The energy contained in each Fourier mode is calculated as $E^{m,n}(t) = \sqrt{[A_x^{m,n}(t)]^2 + [A_y^{m,n}(t)]^2}$ and $E_{\text{total}}(t) = \sum_{m,n} E^{m,n}(t)$. In Fig. 4, we showed the role of Φ on the flow modes of Pr < 1 and Pr > 1. Figure 4(a) (at Pr $= 4.3$ and $\Phi = 0$) shows both (1,1) and (1,3) modes are dominant most of the time, containing nearly 70% of the energy, except during a chaotic state which persists from $19800D/U$ to $19930D/U$. During this chaotic state, other modes energy, such as (1,2), (2,1), (2,2), and (2,3), increase. For $\Phi = 2\pi/9$ [see Fig. 4(b)], the six modes (1,2), (1,3), (2,2), (2,3), (3,2), and (3,3) each contain nearly 15% of energy with minor variations and represents a multiroll state. For $\Phi = \pi/2$, the mode (1,3) is dominant and represents stratification. In the case of Pr $= 0.1$ and $\Phi \leqslant 2\pi/9$, mode (1,1) is dominant and represents a single roll structure without any flow reversal. Beyond $\Phi \geqslant \pi/3$, flow is in a multiroll state with each of the six modes

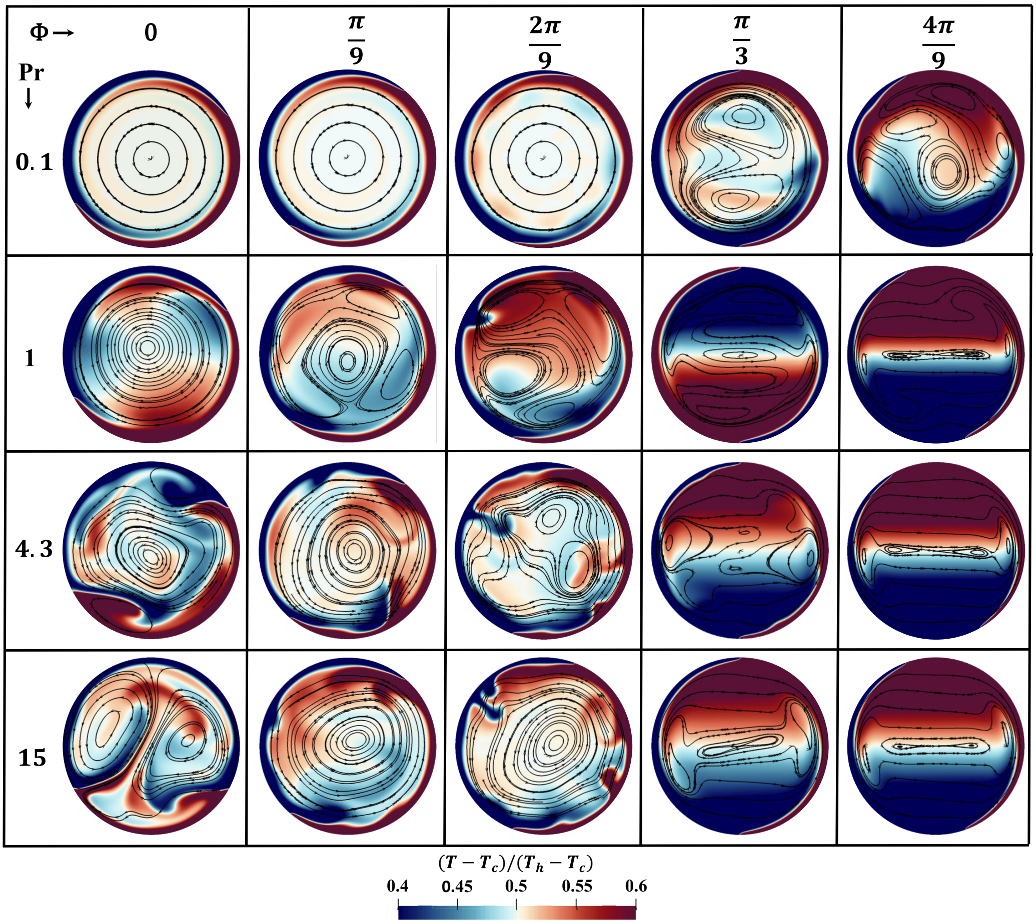

FIG. 3. Instantaneous temperature field (color contours), velocity vectors, and streamlines in a circular enclosure for $\mathrm{Ra} = 10^7$. Colors for temperature vary linearly from 0.4 (blue) to 0.6 (red). Simulations for $\mathrm{Pr} = 0.1$–15 and $0 \leqslant \Phi \leqslant \pi/2$.

(1,2), (1,3), (2,2), (2,3), (3,2), and (3,3) containing nearly 15% energy. The time-averaged energy content of the first nine Fourier modes as a function of Φ is shown in the Appendix (see Fig. 14).

Overall flow features in a circular convection enclosure depend on Ra, Pr, and Φ, and a detailed flow regime map (see Fig. 5) consists of five dominant flow states, such as the single roll, tri-roll, multiroll, chaotic, and the stratified flow. In the case of $\Phi = 0$ and $\mathrm{Pr} \leqslant 1$, flow is in a single-roll state irrespective of Ra, and beyond a critical value of Φ, flow changes to a multiroll state. The critical value of Φ increases with Ra for low Pr ($\leqslant 1$) and decreases with Ra for high Pr (> 1). The tri-roll state at low Ra ($\approx 10^7$), $\mathrm{Pr} = 4.3$ and $\Phi = 0$, is replaced by a single-roll state at high Ra ($\geqslant 10^9$). For $\mathrm{Pr} \geqslant 7$, $\mathrm{Ra} = 10^7$, and $\Phi = 0$, the flow exhibits a chaotic state, transitioning to a tri-roll and eventually to a single-roll state as Ra increases. For intermediate inclination angles ($\pi/9 \leqslant \Phi \leqslant \pi/3$), the multiroll state is primarily visible, and for $\Phi > \pi/3$, the stratified zone sets in.

The flow reversal phenomenon in thermal convection is quite a fascinating topic and is observed in cubical and rectangular boxes [57,59,60], cylinders [61,62], and other geometries [42,43,50]. In 2D enclosures, the flow reversals are explained via different mechanisms such as the metastable equilibrium [63], spontaneous symmetry breaking [64], the corner roll growth and merging [59], vortex reconnection [57], and the giant plume ejection [42,50]. In the case of a classical square

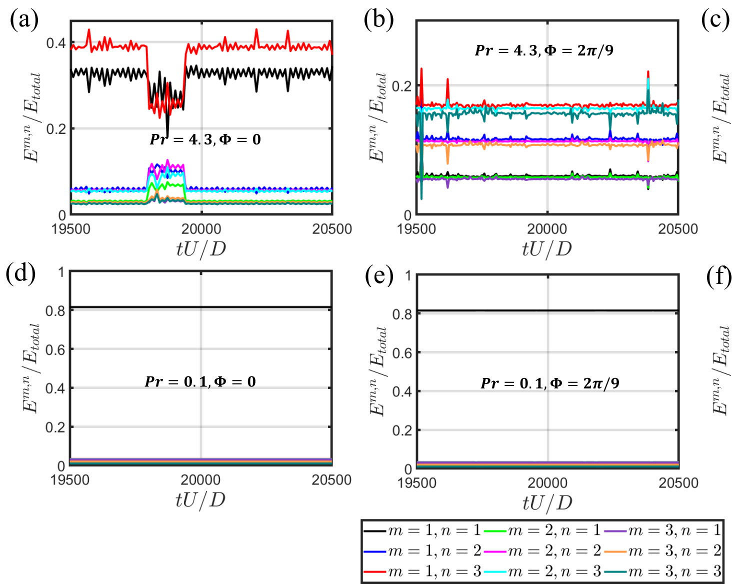

FIG. 4. Time evolution of Fourier energy contained in the first nine Fourier modes for Ra $= 10^7$: (a) Pr $=$ 4.3, $\Phi = 0$; (b) Pr $= 4.3$, $\Phi = 2\pi/9$; (c) Pr $= 4.3$, $\Phi = \pi/2$; (d) Pr $= 0.1$, $\Phi = 0$; (e) Pr $= 0.1$, $\Phi = 2\pi/9$; and (f) Pr $= 0.1$, $\Phi = \pi/2$. Scale of $E^{m,n}/E_{\text{total}}$ varies from 0 to 0.45 for (a) and (c), 0 to 0.3 for (b) and (f), and 0 to 1 for (d) and (e).

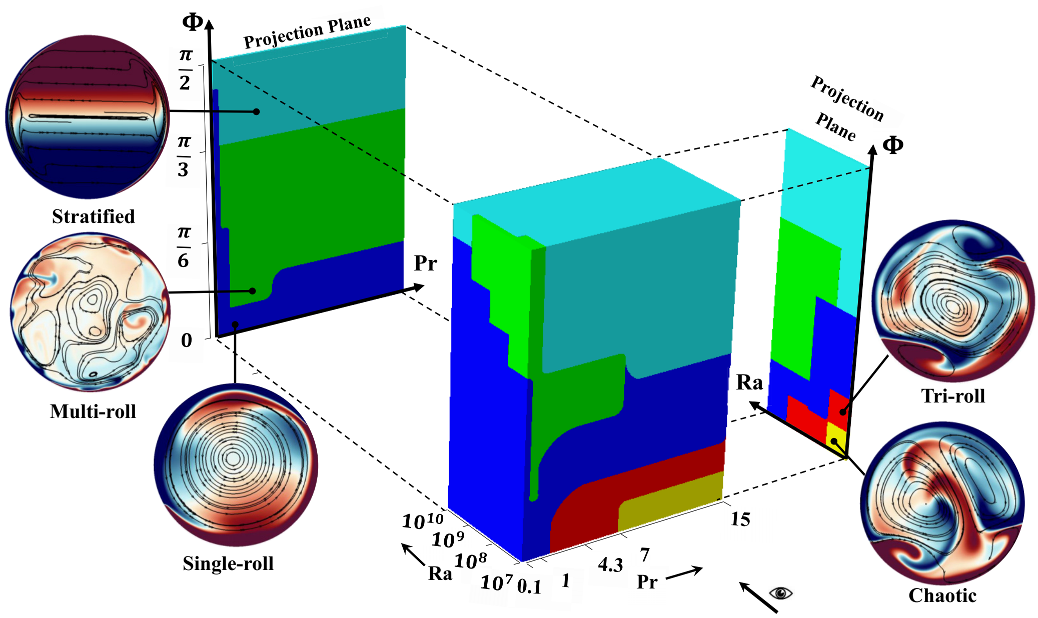

FIG. 5. Flow regime map on the Ra-Pr-Φ plane. Blue region for the single-roll state, red for the tri-roll state, yellow for the chaotic state, green for the multiroll state, and cyan for the stratified flow. Projection planes are shown for clarity, and instantaneous flow features are indicated.

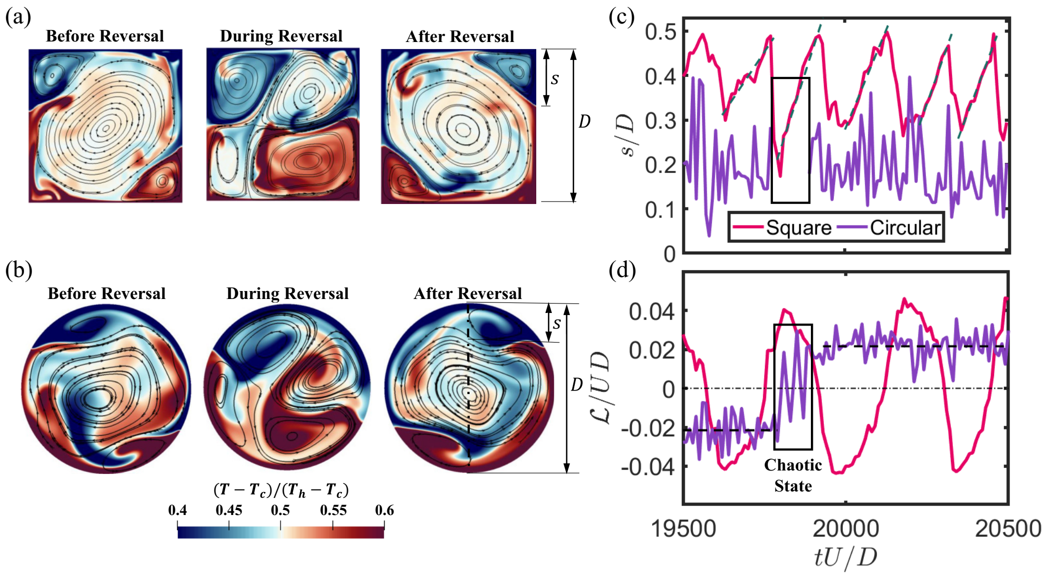

FIG. 6. Flow reversal and secondary roll growth in thermal convection: (a) square and (b) circular enclosure. Color contours for instantaneous dimensionless temperature $(T - T_c)/(T_h - T_c)$, with velocity vectors and streamlines. During a reversal, the quadrupole mode appears in the square enclosure, whereas the massive thermal plumes erupt in the circular enclosure. Time series of secondary roll length (s) and area-averaged angular momentum ($\mathcal{L}$) in panels (c) and (d), respectively. Continuous lines: pink for square and purple for circular enclosure. Dashed lines to show trends.

enclosure, for $\mathrm{Ra} = 10^7$ and $\mathrm{Pr} = 4.3$, in our simulation we observe a diagonally oriented LSC or the primary roll supported by two small counter-rotating secondary rolls at the corners similar to the previous studies [57,59] (see Fig. 6). The secondary rolls grow with time due to trapped thermal plumes, and initiate flow reversals by destroying the primary LSC. As a result, another LSC in the opposite direction is created, and the process repeats with time [57]. The secondary roll grows roughly linear with time before reaching half the height of the enclosure [59]. To compute such a growth rate, first, we excluded the LSC and the wall layers based on the temperature and retained the remaining corner roll zones. The total area of the retained corner roll (A_c) is approximated as an isosceles right angle triangle of length s $(= \sqrt{2A_c})$, and its temporal variation $|ds/dt|$ $(\approx 0.001U)$ is computed. We observed flow reversals take place for every $180D/U$ duration. In the case of a circular RB convection, we observed a primary roll at the center, supported by two counter-rotating secondary rolls at the wall, which are not locked at any particular location but move around the circumference with time (see Movie 1 provided in the Supplemental Material [56]). The initial quiescent fluid destabilizes, and massive-sized hot and cold plumes detach from the walls. The interaction between the massive hot and cold plumes leads to churning of the bulk zone, which sets clockwise and counter-clockwise rotation. A stable LSC is formed when one of the rotations prevails over the other. In that stable LSC state, plumes detach from conduction walls with heat, get trapped in the secondary rolls, and the growth of secondary rolls is observed. Massive plumes erupt alternatively to release the accumulated heat, and their competition sets the circulation into an intermittent (metastable) chaotic state, followed by a stable LSC state in the opposite direction. Our observations on circular convection are consistent with an earlier study [43]. Note that the secondary roll growth does not show any linear trend [see Fig. 6(c)], where discontinuity in the curve is due to the presence of the chaotic state.

To study flow reversals, one of the best indicators is the area-averaged (or global) angular momentum per unit mass $\mathcal{L} = \langle \mathbf{r} \times \mathbf{u} \rangle = \langle xv - yu \rangle$ as a function of time. Previous works [59,65]

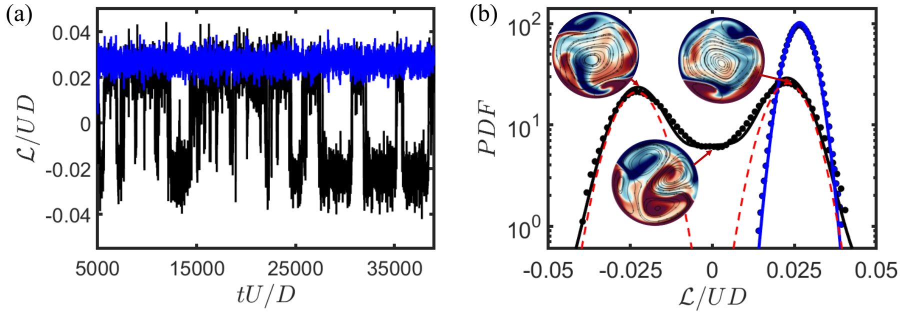

FIG. 7. (a) $\mathcal{L}$ vs time and (b) PDF of $\mathcal{L}$. Lines for $\Phi = 0$ (black) and $\pi/18$ (blue). Double-peak PDF in the case of flow reversals, and a single positive peak for the counterclockwise circulation state without reversals. Snapshots of flow fields at corresponding $\mathcal{L}$. Simulations for $\mathrm{Ra} = 10^7$ and $\mathrm{Pr} = 4.3$. Color contours for the dimensionless temperature field linearly vary from 0.4 (blue) to 0.6 (red). Red dashed lines are two independent Gaussian functions.

reported flow reversals in square cells, represented by the change in the global angular momentum sign. In the square enclosure [59], the flow reversals are inherently connected with secondary roll growth. In circular convection, flow reversals happen in the range $10^7 \leqslant \mathrm{Ra} \leqslant 10^8$ due to the growth of top and bottom secondary rolls [43], and for high $\mathrm{Ra} = 6.2 \times 10^9$, due to massive plume ejections [42]. We have computed $\mathcal{L}$ vs time for both square and circular enclosures to compare the reversal phenomenon in Fig. 6(d). The nearly sinusoidal variation in $\mathcal{L}$ observed in the case of a square RB corresponds to the gradual secondary roll growth and merging, followed by a flow reversal. In contrast, we observe an abrupt variation in $\mathcal{L}$ in the case of a circular RB due to the massive plume interaction-based reversal. To elucidate the role played by Φ, we have shown $\mathcal{L}$ vs time and its probability density function (PDF) at a fixed $\mathrm{Ra} = 10^7$ and $\mathrm{Pr} = 4.3$ in Fig. 7. For $\Phi = 0$, the PDF is a double Gaussian with most probable peaks at $\mathcal{L} = -0.025UD$ and $0.025UD$. The positive $\mathcal{L}$ represents the counterclockwise rotation, and the negative for the clockwise rotation. The chaotic state coexists with the clockwise and counterclockwise circulation states, and the corresponding PDF from their joint effects is the convolution of the PDFs of the two dependent states (circulation state and chaotic state). With a tiny increment in Φ ($\approx\pi/90$), the massive plume ejections are controlled, though spontaneous reversals do persist. With a further increase in Φ ($\geqslant\pi/45$), the prominence of secondary rolls diminishes, flow reversals cease, and a stable LSC forms, which is inferred from the single peak Gaussian curve with a mean value different from zero.

In the case of 2D square enclosures, the reversals are not possible at low Pr ($\leqslant 0.7$) and high $Ra(>10^9)$ and they are observed within the boundaries $Pr \sim Ra^{3/5}$ and $Pr \sim Ra^{2/3}$ on $Ra - Pr$ plane [59]. Recently, Xu *et al.* [43] have shown that flow reversals are possible in circular geometries in the range $10^7 \leqslant \mathrm{Ra} \leqslant 10^8$ and $3 \leqslant \mathrm{Pr} \leqslant 15$. Figures 8(a)–8(d) show the range of Ra–Pr for which the flow reversals take place in circular enclosures for different Φ. Our simulations show that flow reversals decrease with an increase in Φ, especially no reversals beyond $\pi/45$. Note, the dashed lines shown in those figures represent the zone in which the flow reversals take place for $\Phi = 0$ (as mentioned in Fig. 18 of Ref. [43]).

IV. GLOBAL FLOW FEATURES AND HEAT TRANSPORT

In the earlier section, we have seen that changes in Ra, Pr, and Φ alter the flow features, significantly affecting the large-scale circulations and the secondary rolls. As a result, two important measures, the Reynolds number (Re) and the Nusselt number (Nu), may vary. To quantify, we have computed the root-mean-square (rms) velocity ($\overline{\langle \mathbf{u}.\mathbf{u}\rangle}^{1/2}$) -based Reynolds number $\overline{\mathrm{Re}}_{\mathrm{rms}} = \overline{\langle \mathbf{u}.\mathbf{u}\rangle}^{1/2} D/\nu$, and the Nusselt number, $\mathrm{Nu}(t)|_{h,c} = [-k\int \frac{\partial T}{\partial \mathbf{n}}|_{h,c}.\mathbf{n}\, dl]/[kl(T_h - T_c)/D]$ at the hot and

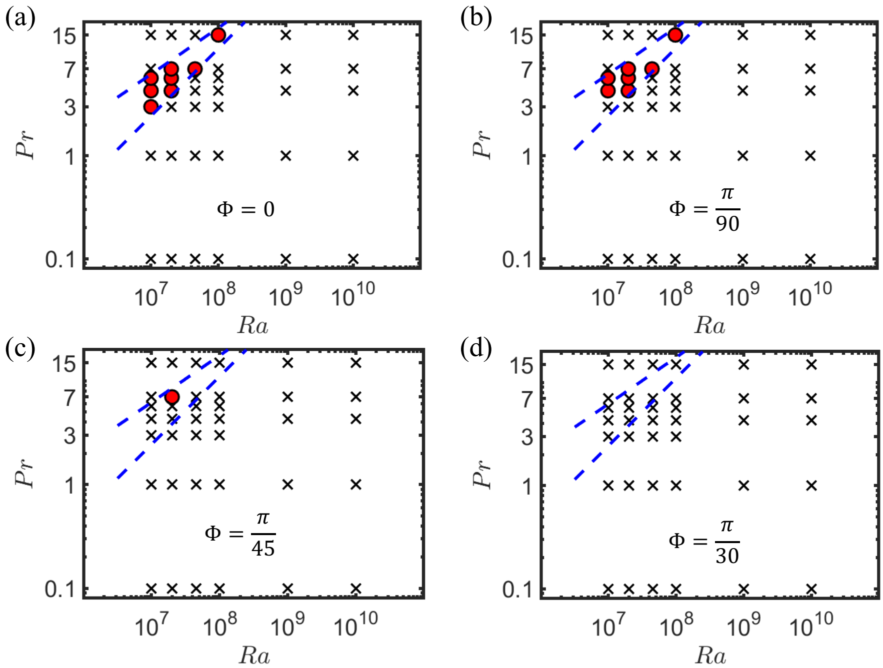

FIG. 8. Phase diagram of flow reversals on the Ra-Pr plane for (a) $\Phi = 0$, (b) $\Phi = \pi/90$, (c) $\Phi = \pi/45$, and (d) $\Phi = \pi/30$. The red circle represents flow reversal and the cross mark represents no flow reversal. Blue dashed lines represent the zone in which the flow reversals take place for $\Phi = 0$.

cold walls along the conduction wall of length (l). Here $\mathbf{n}$ is the wall-normal direction and suffixes h and c denote hot and cold, respectively. The average heat transport at any time in the enclosure is taken as $\mathrm{Nu}(t) = \frac{1}{2}[\mathrm{Nu}(t)|_h + \mathrm{Nu}(t)|_c]$.

In Fig. 9, we have shown time-averaged heat transport ($\overline{\mathrm{Nu}}$) and the rms Reynolds number ($\overline{\mathrm{Re}}_{\mathrm{rms}}$) as functions of Φ. Our results follow polynomial fits, in the form $\overline{\mathrm{Nu}}(\Phi) = \overline{\mathrm{Nu}}(0)(1 + a\Phi + b\Phi^2 + c\Phi^3)$, and $\overline{\mathrm{Re}}_{\mathrm{rms}}(\Phi) = \overline{\mathrm{Re}}_{\mathrm{rms}}(0)(1 + d\Phi + e\Phi^2 + f\Phi^3)$, for the considered range of Ra and Pr. We tabulated the coefficients a, b, c, d, e, and f and compared our results with other works (see Table II). The nonmonotonic trend is better captured via the cubic polynomial curves. The observed nonmonotonic trend can be understood for small and large values of Φ by seeking the limits. The curves of $\overline{\mathrm{Nu}}(\Phi)/\overline{\mathrm{Nu}}(0)$ show different trends for small Pr (<1) and large Pr (>1) [see Figs. 9(c) and 9(d)]. In the case of $\mathrm{Pr} < 1$, $\overline{\mathrm{Nu}}$ increases with Φ and the global maxima of $\overline{\mathrm{Nu}}$ is obtained at $\Phi \approx \pi/6$ [shown by the light-blue patch in Fig. 9(a)] where the strong flow takes place near the walls. For small Φ, the best approximation is $\overline{\mathrm{Nu}}(\Phi) \approx \overline{\mathrm{Nu}}(0)(1 + a\Phi)$, whereas beyond $\Phi > \pi/6$, $\overline{\mathrm{Nu}}(\Phi)$ follows $\overline{\mathrm{Nu}}(\Phi) \approx \overline{\mathrm{Nu}}(0)(1 + b\Phi^2)$, where b is the negative coefficient.

For $\mathrm{Pr} = 4.3$, $\mathrm{Ra} < 10^9$, and $\Phi = 0$, the primary roll is supported by the two secondary rolls, which inhibit plume detachment. These secondary rolls gradually get eliminated with increasing Φ, and heat transfer linearly increases, $\overline{\mathrm{Nu}}(\Phi) \approx \overline{\mathrm{Nu}}(0)(1 + a\Phi)$, for small Φ [see Fig. 9(c)]. For the same Pr, but at $\mathrm{Ra} = 10^{10}$, the presence of strong LSC is weakened with an increase in Φ and results in linear decrement in $\overline{\mathrm{Nu}}(\Phi)$ described by $\overline{\mathrm{Nu}}(\Phi) \approx \overline{\mathrm{Nu}}(0)(1 + a\Phi)$, where a is the negative coefficient. With a further increase in Φ, when multiroll structures are formed, $\overline{\mathrm{Nu}}(\Phi)$ starts increasing and attains maxima due to efficient mixing of bulk. In this zone, linear term $a\Phi$ and higher-order terms $b\Phi^2$ and $c\Phi^3$ are comparable. Further inclination ($\Phi > 7\pi/18$) leads to a decrease in global heat transport due to the stratification effect, which is described by the polynomial function $\overline{\mathrm{Nu}}(\Phi) \approx \overline{\mathrm{Nu}}(0)(1 + c\Phi^3)$, where c is the negative coefficient. The heat

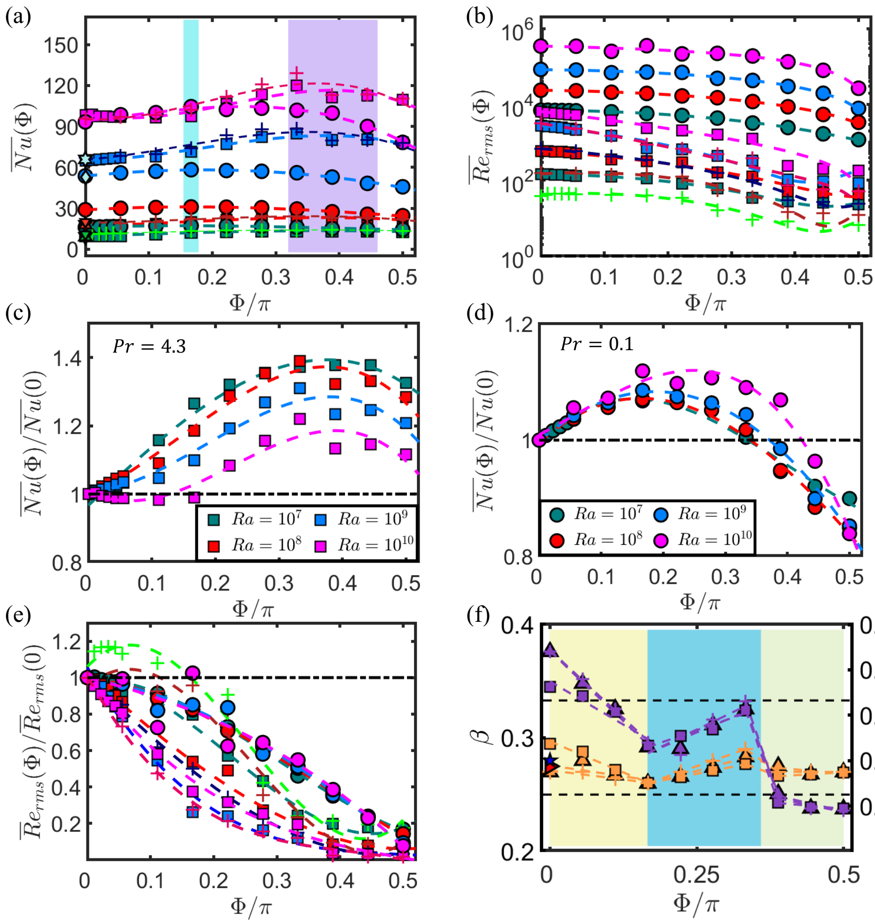

FIG. 9. As a function of Φ: (a) $\overline{\mathrm{Nu}}$, (b) $\overline{\mathrm{Re}}_{\mathrm{rms}}$, $\overline{\mathrm{Nu}}(\Phi)/\overline{\mathrm{Nu}}(0)$ for (c) $\mathrm{Pr} = 4.3$, (d) $\mathrm{Pr} = 0.1$, (e) $\overline{\mathrm{Re}}_{\mathrm{rms}}(\Phi)/\overline{\mathrm{Re}}_{\mathrm{rms}}(0)$, and (f) $\overline{\mathrm{Nu}}$ scaling exponents (orange) and $\overline{\mathrm{Re}}_{\mathrm{rms}}$ scaling exponents (purple). Symbols are for $\mathrm{Pr} = 0.1$ (circle), $\mathrm{Pr} = 4.3$ (square), $\mathrm{Pr} = 7$ (triangle), and $\mathrm{Pr} = 15$ (plus). Colors are for $\mathrm{Ra} = 10^7$ (green), $\mathrm{Ra} = 10^8$ (red), $\mathrm{Ra} = 10^9$ (blue), and $\mathrm{Ra} = 10^{10}$ (magenta). Dashed lines for the best cubic fits. Dash-dotted line at 1 in panels (c), (d), and (e). The two black dashed lines for 1/3 and 1/4 in panel (f) are to guide the eye. Additional symbols: hexagram ($\mathrm{Pr} = 4.3$), inverted triangle ($\mathrm{Pr} = 15$) [43], diamond ($\mathrm{Pr} = 0.1$) [49] for $\overline{\mathrm{Nu}}$ and right-pointing triangle [41], and pentagram [42] for $\overline{\mathrm{Nu}}$ scaling exponents from earlier works.

transport dependence on Φ in the circular enclosure qualitatively resembles the results of inclined cylinders with $\Gamma = 1$ and $1/5$ [31,32] where for $\mathrm{Pr} > 1$, $\overline{\mathrm{Nu}}(\Phi)$ increases with Φ until $\Phi \approx 0.4\pi$, reaches maxima and decreases with further increase in Φ. On the other hand, for $\mathrm{Pr} < 1$, $\overline{\mathrm{Nu}}(\Phi)$ increases with Φ and global maxima is obtained for the intermediate value of Φ. In the case of the rectangular enclosure [36,39,66], $\overline{\mathrm{Nu}}(\Phi)$ shows completely different behavior than cylinders and the circular enclosure, both in terms of nonmonotonic trend and maxima. Our results on $\overline{\mathrm{Re}}_{\mathrm{rms}}(\Phi)$ show that the overall enclosure's convective motions decrease with an increase in Φ. Though the thermal plumes preferably move along the wall with an increase in Φ, their area is less compared to the quiescent bulk zone. As a result, a decrease in $\overline{\mathrm{Re}}_{\mathrm{rms}}$ with Φ is observed. For $\mathrm{Pr} \leqslant 1$, $\overline{Re}_{\mathrm{rms}}$ increases for small Φ $(= \pi/90)$ and decreases beyond $\Phi \geqslant \pi/45$ similar to the inclined cylinder [32] where an initial increase of $\overline{\mathrm{Re}}$ with Φ is related to unsteady convection and efficient buoyancy-induced mixing of bulk.

TABLE II. Comparision of heat transport and rms Reynolds numbers for different geometries. Best fits in the form of $\overline{\mathrm{Nu}}(\Phi) = \overline{\mathrm{Nu}}(0)(1 + a\Phi + b\Phi^2 + c\Phi^3)$ and $\overline{\mathrm{Re}}_{\mathrm{rms}}(\Phi) = \overline{\mathrm{Re}}_{\mathrm{rms}}(0)(1 + d\Phi + e\Phi^2 + f\Phi^3)$. Fit parameters are a, b, c, d, e, and f. The rows are for different works and polynomial coefficients in a given range of Ra, Pr, and Φ.

Case	Ra, Pr	Φ	a	b	c	d	e	f
Cylinder ($\Gamma = 0.5$) [33]	10^{12}, 4	$0 \leqslant \Phi \leqslant 0.01\pi$	−2	0	0			
Cylinder ($\Gamma = 1$) [34]	10^{11}, 4	$0 \leqslant \Phi \leqslant 0.04\pi$	−0.031	0	0			
Square [36]	10^9, 6	$0 \leqslant \Phi \leqslant 0.048\pi$	−0.27	0	0			
		$0.048\pi \leqslant \Phi \leqslant 0.334\pi$	−0.103	0	0			
		$0.334\pi \leqslant \Phi \leqslant 0.5\pi$	−0.754	0	0			
Rectangle ($\Gamma = 0.5$) [66]	10^7, 0.1	$0 \leqslant \Phi \leqslant 0.5\pi$	0.103	0.37	−0.051	0.37	−0.67	0.11
	10^7, 4.38		0.13	0.68	−0.37	0.58	−1.47	0.53
Cylinder ($\Gamma = 1/5$) [31]	10^7, 0.1	$0 \leqslant \Phi \leqslant 0.5\pi$	3.29	−1.85	−0.06	1.32	−0.74	−0.13
	10^8, 0.1		1.37	−0.37	−0.22	0.56	−0.054	−0.31
	10^9, 0.1		1.14	−0.99	0.24	0.55	−0.29	−0.19
	10^8, 1		1.65	−2.28	0.79	1.33	−1.93	0.52
	10^9, 1		1.14	−0.94	0.18	0.77	−0.99	0.11
Cylinder ($\Gamma = 1$) [32]	10^7, 1	$0 \leqslant \Phi \leqslant 0.5\pi$	0.24	−0.22	0.046	0.12	−0.8	0.27
	10^8, 1		0.28	−0.22	0.025	0.17	−0.81	0.24
Quasi-2D circular (our simulations)	10^7, 0.1	$0 \leqslant \Phi \leqslant 0.5\pi$	0.35	−0.46	0.12	0.012	−0.76	0.27
	10^{10}, 0.1		0.18	0.083	−0.17	−0.25	−0.15	−0.04
	10^7, 4.3		0.57	−0.048	−0.11	0.057	−1.34	0.62
	10^{10}, 4.3		−0.3	0.84	−0.39	−1.46	0.76	−0.15
	10^7, 15		0.34	0.006	−0.089	1.18	−3.22	1.36
	10^{10}, 15		−0.069	0.74	−0.41	−1.96	1.42	−0.37

From our simulations, we find the scaling laws in the form $\overline{\mathrm{Nu}} \propto \mathrm{Ra}^{\beta}$ and $\overline{\mathrm{Re}}_{\mathrm{rms}} \propto \mathrm{Ra}^{\gamma}$, where $1/4 \leqslant \beta \leqslant 1/3$ and $0.3 \leqslant \gamma \leqslant 0.64$ for the considered Ra and Pr range. For RB convection in a 2D square enclosure, the exponents range as $0.285 \leqslant \beta \leqslant 0.3$ and $0.59 \leqslant \gamma \leqslant 0.62$ for $10^6 \leqslant \mathrm{Ra} \leqslant 10^{12}$ and $0.7 \leqslant \mathrm{Pr} \leqslant 5.3$ [65,67,68]. Experimental measurements of quasi-2D circular enclosure [41,42] show $\beta \approx 0.28$ and $\gamma \approx 0.49$ at $\Phi = 0$, and our results indeed agree with the reported values [see Fig. 9(f)]. Both the exponents show nonmonotonic trends with Φ. The exponents decrease up to $\Phi < 0.2\pi$ due to the gradual elimination of secondary rolls, and increase between $0.2\pi \leqslant \Phi \leqslant 0.33\pi$ due to bulk core instabilities, and show a sharp jump to nearly constant values for $\Phi > 0.33\pi$ in the stratified zone. Note the reported global scaling laws, though useful for many engineering applications, have limitations in revealing insight into local flow dynamics and must be used carefully.

A. Scaling-analysis-based estimation of Nu and Re

To get more insight on $\mathrm{Nu}(\Phi)$ and $\mathrm{Re}(\Phi)$, here we have constructed a transient scaling analysis [19,69] in terms of the 2D cylindrical polar coordinates (r, θ) and the velocity $\mathbf{u} = (u_r, u_\theta)$ [see Fig. 1(b)]. Note the enclosure inclination (Φ) is measured with respect to the negative y axis, and the gravity is $\mathbf{g} = (g_r, g_\theta) = (-g\cos\Phi, -g\sin\Phi)$. The conservation of mass, momentum, and thermal energy equations, in the explicit form, are mentioned in the Appendix, from Eq. (A1) to Eq. (A4).

We consider zero initial velocity field and seek growth of the thermal boundary layer with time. The applied temperature difference ΔT $(\equiv T_h - T_c)$ helps the thermal boundary-layer thickness, δ_T (measured next to the conduction wall in the radial direction), to grow in time τ_d. By balancing the thermal inertia with the conduction, i.e., $\frac{\partial T}{\partial t} \sim \kappa \frac{1}{r}\frac{\partial}{\partial r}(r\frac{\partial T}{\partial r})$, gives us $\delta_T \sim \sqrt{\kappa \tau_d}$. The boundary

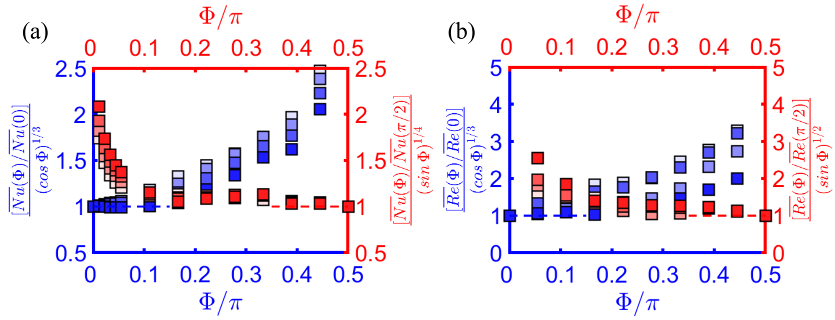

FIG. 10. As a function of Φ: (a) compensated $\overline{\mathrm{Nu}}$ and (b) compensated $\overline{\mathrm{Re}}$ based on time-averaged local velocity at the thermal boundary layer for $\mathrm{Pr} = 4.3$. Left (blue) and right (red) y axes scale differently. Shades of blue and red colors vary from light to dark with increasing Ra as 10^7, 10^8, 10^9, and 10^{10}. The dashed line at 1 is to guide the eye.

layer further grows as the buoyancy increases, and as a result, the fluid convects along the wall. The (transient) velocity component is obtained by balancing the fluid inertia with the buoyancy and the viscous terms. A better choice is to first eliminate the pressure by subtracting $\frac{\partial}{\partial\theta}$ of Eq. (A2) from $\frac{\partial}{\partial r}$ of r times Eq. (A3). For small Φ, the balance between inertia, viscosity, and buoyancy corresponds to $\frac{\partial}{\partial\theta}(\frac{\partial u_r}{\partial t}) \sim \nu\frac{\partial}{\partial\theta}[\frac{1}{r}\frac{\partial}{\partial r}(r\frac{\partial u_r}{\partial r})] \sim \frac{\partial}{\partial\theta}(g_r\alpha[T - T_m])$, which gives $\frac{u_r}{t} \sim \frac{\nu u_r}{\delta_T^2} \sim g_r\alpha\Delta T$. For large Φ we have $\frac{\partial}{\partial r}(r\frac{\partial u_\theta}{\partial t}) \sim \nu\frac{\partial^2}{\partial r^2}(r\frac{\partial u_\theta}{\partial r}) \sim \frac{\partial}{\partial r}(g_\theta r\alpha[T - T_m])$, which gives $\frac{u_\theta}{t} \sim \frac{\nu u_\theta}{\delta_T^2} \sim g_\theta\alpha\Delta T$. Note the balance is applicable to any convective time $t > \tau_d$. In the boundary layer, the viscous effects are also important and not negligible; thus, the relative importance of the buoyancy and the inertia with respect to the viscous forces, obtained respectively as $\frac{\mathcal{G}\alpha\Delta T\delta_T^2}{\nu u_c}$ and $1/\mathrm{Pr}$. Here, the gravity-related factor $\mathcal{G}$ equals to g_r and characteristic velocity $u_c = u_r$ for small Φ and to g_θ and u_θ, respectively, for large Φ. Note that the convection does not set in unless the buoyancy is greater than the viscous forces. The mentioned comparison between the forces is strictly applicable as long as the viscous forces are finite and not negligible, which requires $\mathrm{Pr} \gg 1$. At the onset of convection, the buoyancy balances the viscous forces, thus $u_r \sim \frac{g_r\alpha\Delta T\delta_T^2}{\nu} \sim (\frac{g_r\alpha\kappa\Delta T}{\nu})t$ (for small Φ) and $u_\theta \sim \frac{g_\theta\alpha\Delta T\delta_T^2}{\nu} \sim (\frac{g_\theta\alpha\kappa\Delta T}{\nu})t$ (for large Φ). As time proceeds, some part of the accumulated thermal energy is carried towards the other wall by thermal inertia, and the remaining part diffuses out of the boundary layer. The mentioned process takes place on a (long) timescale $t = \tau_c$ ($\gg \tau_d$), which can estimated as $\frac{\Delta T}{\tau_c} \sim \frac{u_r\Delta T}{\delta_T} \sim \frac{\kappa\Delta T}{\delta_T^2}$ for small Φ, and $\frac{\Delta T}{\tau_c} \sim \frac{u_\theta\Delta T}{D} \sim \frac{\kappa\Delta T}{\delta_T^2}$ for large Φ; thus, $\tau_c \sim (\nu/[g_r\alpha\sqrt{\kappa}\Delta T])^{2/3}$ for small Φ and $\tau_c \sim \sqrt{(\nu D/[g_\theta\alpha\kappa\Delta T])}$ for large Φ. At a steady state, the boundary-layer thickness does not grow and follows $\delta_T \sim \sqrt{\kappa\tau_c}$, which means δ_T proportional to $D(\mathrm{Ra}\cos\Phi)^{-1/3}$ at small Φ and $D(\mathrm{Ra}\sin\Phi)^{-1/4}$ at large Φ. A perfect balance between the thermal convection with diffusion (from the energy equation) and also the buoyancy with the viscous forces (in the momentum equation) coexists. The heat flux that leaves the conduction wall is estimated as $\rho c\kappa\nabla T \sim \rho c\kappa\Delta T/\delta_T$ and thus the dimensionless heat transport is proportional to $\frac{D}{\delta_T} \sim (\mathrm{Ra}\cos\Phi)^{1/3}$ at small Φ and to $(\mathrm{Ra}\sin\Phi)^{1/4}$ at large Φ. Note, the dimensionless heat transport is inversely proportional to the thermal boundary-layer thickness, thus we have $\mathrm{Nu} \sim \mathrm{Ra}^{1/3}$ at $\Phi = 0$ and $\mathrm{Nu} \sim \mathrm{Ra}^{1/4}$ at $\Phi = \pi/2$ which gives $\mathrm{Nu}(\Phi) \sim \mathrm{Nu}(0)(\cos\Phi)^{1/3}$ for small Φ and $\mathrm{Nu}(\Phi) \sim \mathrm{Nu}(\pi/2)(\sin\Phi)^{1/4}$ for large Φ. In Fig. 10(a), we have shown the simulation-based $\overline{\mathrm{Nu}}(\Phi)/\overline{\mathrm{Nu}}(0)$ and $\overline{\mathrm{Nu}}(\Phi)/\overline{\mathrm{Nu}}(\pi/2)$. Interestingly, the numerical simulations based on $\overline{\mathrm{Nu}}$ in the range $0 \leqslant \Phi < \pi/9$ follow the scaling law $\mathrm{Nu}(\Phi) \sim (\mathrm{Ra}\cos\Phi)^{1/3}$ while in the range $\pi/9 \leqslant \Phi \leqslant \pi/2$ they follow the scaling law $\mathrm{Nu}(\Phi) \sim (\mathrm{Ra}\sin\Phi)^{1/4}$. Similarly, we have estimated the Reynolds number based on velocity at the onset of the convection as $\frac{u_r D}{\nu} \sim \frac{(\mathrm{Ra}\cos\Phi)^{1/3}}{\mathrm{Pr}}$ for small Φ and

$\frac{u_\theta D}{\nu} \sim \frac{(\text{Ra} \sin \Phi)^{1/2}}{\text{Pr}}$ for large Φ. Re_{rms}, which is calculated in Sec. IV, is based on rms velocity, which is not equivalent to the velocity at the onset of the convection, and we cannot compare our scaling-based Re with Re_{rms}. In scaling analysis, the velocity at the onset of the convection is derived by balancing buoyancy and viscous forces. In buoyancy-driven thermal convection, thermal plumes start forming at the boundary layer when buoyancy balances the viscous force, and outside the boundary layer plumes are carried away by inertia. Thus, the velocity of plumes at the boundary layer is equivalent to the velocity at the onset of the convection. Therefore, we calculated the Reynolds number ($\overline{\text{Re}}$) based on time-averaged local velocity at the thermal boundary layer, which is computed on the midline [see double arrow line in Fig. 1(b)] coinciding with the applied thermal gradient and showed the compensated $\overline{\text{Re}}$ in Fig. 10(b). Our simulation-based $\overline{\text{Re}}(\Phi)$ in the range $0 \leqslant \Phi \leqslant \pi/9$ follows the scaling law $\text{Re}(\Phi) \sim \frac{(\text{Ra} \cos \Phi)^{1/3}}{\text{Pr}}$ while in the range $\pi/9 \leqslant \Phi \leqslant \pi/2$ it follows the scaling law $\text{Re}(\Phi) \sim \frac{(\text{Ra} \ \sin \Phi)^{1/2}}{\text{Pr}}$.

B. Comparison of the velocity and temperature fields

With an increase in Φ, our results show $\overline{\text{Re}}_{\text{rms}}$ decreases, whereas $\overline{\text{Nu}}$ shows a nonmonotonic trend combining linear increment at small Φ and quadratic and cubic decrement at large Φ. To understand this, we have computed the rms velocity $U_{\text{rms}} = (\overline{\mathbf{u} \cdot \mathbf{u}})^{1/2}$ and temperature $T_{\text{rms}} = (\overline{T^2})^{1/2}$ in the radial direction coinciding with the applied thermal gradient [see Figs. 11(a) and 11(b)]. For $\text{Ra} = 10^7$, $\text{Pr} = 4.3$, and $\Phi = 0$, the U_{rms} profile shows two peaks, indicating the existence of both the primary and the secondary rolls. Near-wall shear motions are observed up to $r = 0.24D$ from the wall. For the same Ra and Pr with an increase in Φ, the plumes move along the walls without entering the bulk zone; thus, a single peak is observed for $\Phi = 2\pi/9$, which is close to the wall. For $\text{Ra} = 10^{10}$, $\text{Pr} = 4.3$, and $\Phi = 0$, we observed a single peak due to strengthened circulation. With an increase in Φ, occasionally, thermal plumes penetrate the bulk zone and trigger baroclinic instabilities in the core bulk zone; hence, we see two distinguished peaks for $\Phi = 2\pi/9$—one near the walls and the other in the core bulk zone. In the case of $\text{Pr} = 4.3$, irrespective of Ra, stratification effects are seen beyond $\Phi > \pi/3$, and the bulk zone becomes quiescent [see Fig. 11(a)]. In the case of $\text{Ra} = 10^7, \text{Pr} = 0.1$, a single roll structure with strong shear motions near the wall is observed up to $\Phi \approx 2\pi/9$, which corresponds to a single peak. Beyond $\Phi > \pi/3$, unlike $\text{Pr} > 1$, considerable velocity fluctuations are seen even in the bulk zone. The strengthened wall motions naturally decrease the thermal boundary-layer thickness, whereas the plume motions in the core bulk zone homogenize the thermal fields. This reduction in the thermal boundary-layer thickness with an increasing Φ is one of the reasons for increasing the $\overline{\text{Nu}}$ with Φ. The nonmonotonic trend in $\overline{\text{Nu}}(\Phi)$ is due to the concentration of plumes near the wall at small Φ, destabilization of core bulk at intermediate Φ, and flow stratification at high Φ.

Based on the rms velocity and the temperature profiles in the radial direction, we have estimated the viscous boundary-layer thickness (δ_u), which is the distance between the wall and the position where the rms velocity reaches its maximum value [see Fig. 11(c)]. Similarly, the thermal boundary-layer thickness (δ_T) is the distance from the wall to the position (extrapolated from the wall thermal gradient) at which the temperature T_{rms} reaches T_m [see Fig. 11(d)]. In the case of $\text{Pr} > 1$, we observe $\delta_T \ll \delta_u$ for small Φ; however, they are comparable at large Φ. On the other hand, in the case of $\text{Pr} < 1$, $\delta_T \gg \delta_u$, with an increase in Φ, δ_u decreases continuously but δ_T decreases up to $\Phi \leqslant \pi/6$, and beyond $\Phi > \pi/6$ increases. With an increase in Φ, the reduction in δ_u is more pronounced compared to the reduction in δ_T, indicating an increase in near-wall shear motions. The strengthened wall shear motions can be further appreciated from the wall-normal gradient of U_{rms} computed (on the double arrow line shown in Fig. 1) at different inclination angles [see Fig. 11(e)]. The velocity gradient is maximum in the range $7\pi/18 \leqslant \Phi \leqslant 4\pi/9$ for $\text{Pr} > 1$ [see the purple patch in Fig. 11(e)] and at $\Phi \approx \pi/6$ for $\text{Pr} < 1$ [see the light-blue patch in Fig. 11(e)]. Indeed, the range of Φ for the maximum velocity gradient coincides with the maximum $\overline{\text{Nu}}$ [see the purple

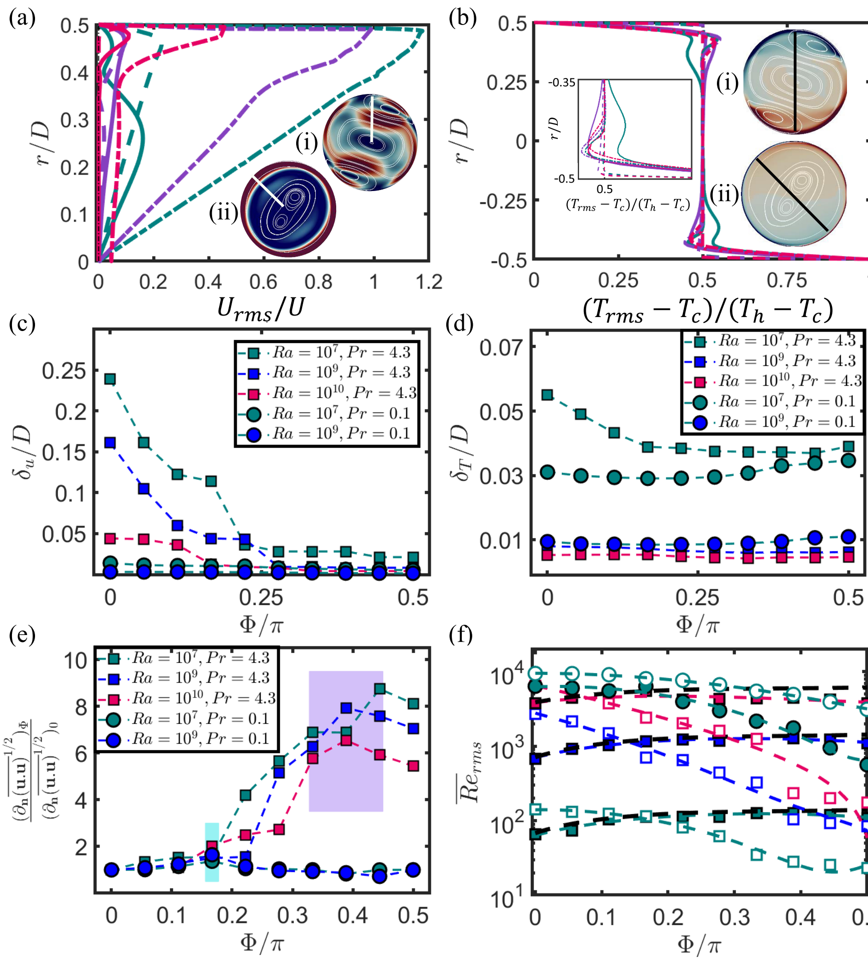

FIG. 11. Time-averaged (a) $U_{\rm rms}$ and (b) $T_{\rm rms}$. Lines for $\mathrm{Pr} = 4.3$, $\mathrm{Ra} = 10^7$ (continuous), $\mathrm{Pr} = 4.3$, $\mathrm{Ra} = 10^{10}$ (dashed), $\mathrm{Pr} = 0.1$, $\mathrm{Ra} = 10^7$ (dash-dotted), and colors for $\Phi = 0$ (green), $\Phi = 2\pi/9$ (purple), and $\Phi = \pi/2$ (pink). Snapshots of $U_{\rm rms}$ and $T_{\rm rms}$ for (i) $\mathrm{Pr} = 4.3$, $\mathrm{Ra} = 10^7$, and $\Phi = 0$, (ii) $\mathrm{Pr} = 4.3$, $\mathrm{Ra} = 10^{10}$, and $\Phi = 2\pi/9$. Line in snapshot along which $U_{\rm rms}$ and $T_{\rm rms}$ are taken. As a function of Φ: (c) velocity, (d) thermal boundary-layer thickness, (e) normalized velocity gradient measured in the velocity boundary layer, and (f) $\overline{\mathrm{Re}}_{\rm rms}$. Open symbols for enclosure averaged $\overline{\mathrm{Re}}_{\rm rms}$ and filled symbols for $\overline{\mathrm{Re}}_{\rm rms}$ measured in the thermal boundary layer. Symbols are for $\mathrm{Pr} = 0.1$ (circle) and $\mathrm{Pr} = 4.3$ (square). Colors are for $\mathrm{Ra} = 10^7$ (green), $\mathrm{Ra} = 10^9$ (blue), and $\mathrm{Ra} = 10^{10}$ (magenta). Black dashed lines for $\overline{\mathrm{Re}}$ scaling relation.

and light-blue patches in Figs. 9(a) and 11(e)]. Also, we see a significant relative increment in velocity gradient with an increase in Φ in the case of $\mathrm{Pr} = 4.3$ and $\mathrm{Ra} = 10^7$, where we observed the maximum increment in $\overline{\mathrm{Nu}}(\Phi)/\overline{\mathrm{Nu}}(0)$. In Fig. 11(f), we have compared the rms based Reynolds number computed inside the thermal boundary layer and the entire enclosure area-averaged $\overline{\mathrm{Re}}_{\rm rms}$ as a function of Φ. For $\mathrm{Pr} < 1$, both $\mathrm{Re}_{\rm rms}$ reduce with Φ. Whereas in the case of $\mathrm{Pr} > 1$ with an increase in Φ, though the enclosure area-averaged $\overline{\mathrm{Re}}_{\rm rms}$ decreases, the $\overline{\mathrm{Re}}_{\rm rms}$ inside the thermal boundary layer increases. We infer from this result that with increasing Φ, small near-wall zones are still involved in the convection process.

V. ENERGY PATHWAYS

In the earlier sections, we have seen that the nonmonotonic trend in $\overline{\mathrm{Nu}}$ is due to increased plume motions near the wall, absence of secondary rolls, presence of core bulk instabilities, and flow stratification. Flow states can be understood better based on the energetics [38,60,70–72]. The buoyancy flux exchanged at the boundaries redistributes into various forms and creates a wide range of spatiotemporal scales. An overall thermodynamic balance is expected at the stationary state [71,72]. At any given instant, the system's state can be characterized by two important quantities: (1) the potential energy, $E_p = \mathrm{g}\int y\rho\, dV$, which is used to lift the fluid to a reference height y_{ref} against gravity, and (2) the kinetic energy, $E_k = (\rho_m/2)\int \mathbf{u}\cdot\mathbf{u}\, dV$, which represents the mechanical contribution. Here, $\int dV$ is the volume integral (for 2D systems, it becomes the area integral). Note the density (ρ) is connected to the local temperature (T) through the Boussinesq approximation. The energy balance in the volume average sense is $\frac{dE_p}{dt} = \phi_y + \phi_{b1} + \phi_i$ and $\frac{dE_k}{dt} = -\phi_y + \phi_\tau - \epsilon$. Here, $\phi_y = \mathrm{g}\int \rho v\, dV$ is the buoyancy flux, $\phi_{b1} = \mathrm{g}\kappa \oint y(\nabla\rho\cdot\mathbf{n})dS$ is the net buoyancy input applied at the hot and the cold walls, $\phi_i = -\mathrm{g}\kappa\int(\Delta\rho/\Delta y)dS$ is the energy required to raise or lower the center of mass due to molecular diffusion irreversibly, $\phi_\tau = \rho_m\nu\oint[\mathbf{u}\cdot(\mathbf{n}\cdot\nabla\mathbf{u})]dS$ is the boundary stress which is zero due to no-slip conditions, and $\epsilon = \rho_m\nu\int|\nabla\mathbf{u}|^2 dV$ is the viscous dissipation. Here, S is the surface with normal $\mathbf{n}$ bounding the volume V.

Note, not all the potential energy of a fluid is available for conversion into kinetic energy. The fraction that remains unavailable for this conversion is termed as the background potential energy, $E_b = \mathrm{g}\int y_{\mathrm{ref}}\rho\, dV$. This background potential energy of a fluid corresponds to a state of no motion or gravitational equilibrium in which fluid parcels have been adiabatically rearranged to new vertical positions $y_{\mathrm{ref}} = y_{\mathrm{ref}}(\rho)$. Conversely, the portion of potential energy amenable to convert into kinetic energy is termed as the available potential energy, E_a ($\equiv E_p - E_b$). The energy can be released and converted to kinetic energy only if some rearrangement of fluid results in lower potential energy [73]. The convective motions are completely driven by the available component, whereas the background component helps to exchange the energy between the terms. The applied thermal gradient at the boundaries converts the background potential energy into the available potential energy, and the irreversible mixing in the temperature field does the opposite. The corresponding evolution equations for the individual potential energy components are $\frac{dE_b}{dt} = -\phi_{b2} + \phi_d$ and $\frac{dE_a}{dt} = \phi_y + \phi_{b1} + \phi_{b2} - \phi_d + \phi_i$. Here $\phi_{b2} = -\mathrm{g}\kappa\oint y_{\mathrm{ref}}(\nabla\rho\cdot\mathbf{n})dS$ is the buoyancy force required to maintain the convection to take place instead of reaching an adiabatically relaxed state, and $\phi_d = -\mathrm{g}\kappa\int(dy_{\mathrm{ref}}/d\rho)(\nabla\rho\cdot\nabla\rho)dV$ is the irreversible mixing which homogenizes the density field. Time averaging of the evolution equation of E_b leads to $\overline{\phi}_{b2} = \overline{\phi}_d$.

To analyze the energy conversions within the circular convection enclosure, we computed E_p, E_b, E_a, E_k and the source (ϕ_{b1} and ϕ_{b2}) and the sink (ϕ_y, ϕ_d, and ϕ_i) terms of E_a. Figure 12(a) shows the detailed energy conversion paths. The red and green lines denote the prominent paths of available potential energy conversion in the $\Phi = 0$ case and the inclined circular enclosure, respectively. Figure 12(b) illustrates the fraction of potential energy converted into the available (E_a) and the background (E_b) potential energy. Notably, the proportion of E_a increases while that of E_b decreases with an increase in Φ. A portion of the available potential energy is utilized by the buoyancy flux to convert it into kinetic energy, while the irreversible mixing and molecular diffusion consume the other portion. To analyze the conversion process, we have shown $\overline{\phi}_y$ and $\overline{\phi}_{b2}$ as a function of Φ [see Figs. 12(c) and 12(d)]. The buoyancy flux decreases with Φ; as a result, the proportional kinetic energy decreases [see Figs. 12(e) and 12(f)], whereas both the irreversible mixing and the molecular diffusion increase. The combined rate of work by buoyancy, $\phi_{b1} + \phi_{b2}$, which sustains the convective flow, increases with Φ. Although the kinetic energy decreases in inclined circular enclosures, convection persists through irreversible mixing. To quantify the dominant path of available potential energy conversion, we calculated the mixing efficiency $\eta = (\overline{\phi}_d - \overline{\phi}_i)/(\overline{\phi}_d - \overline{\phi}_i + \overline{\epsilon})$ which measures the portion of available potential energy used for irreversible mixing [see Fig. 12(g)]. For $\Phi = 0$, we obtained $\eta \approx 0.5$, which means both buoyancy

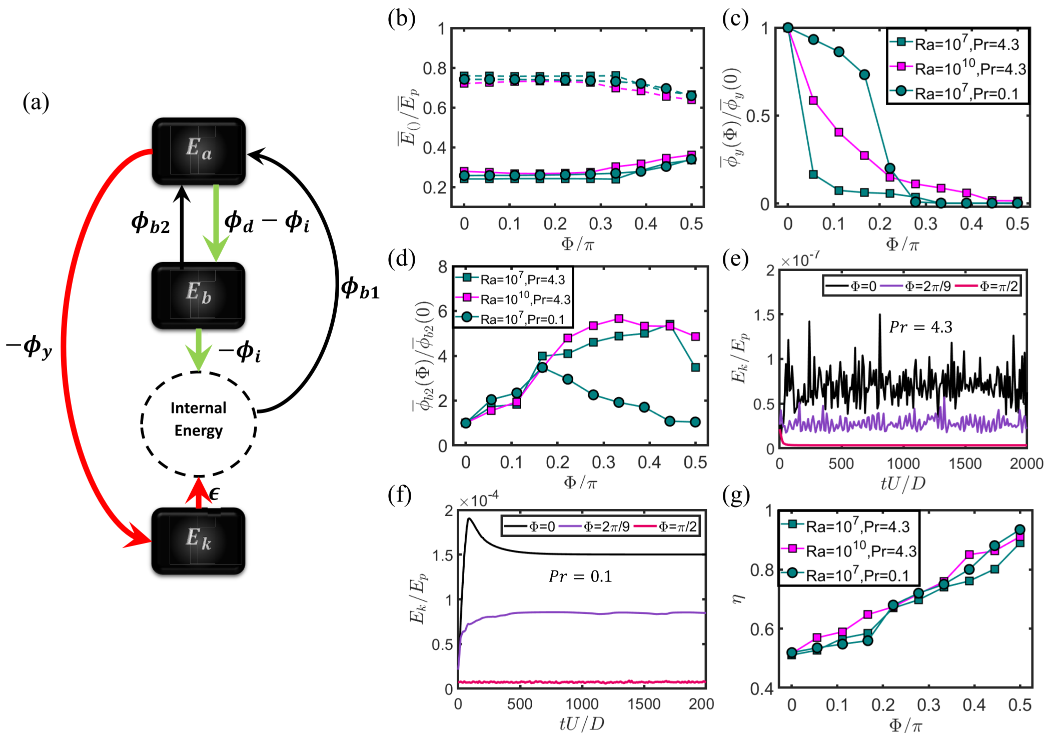

FIG. 12. (a) Schematics of energy paths in thermal convection. Red (for $\Phi = 0$) and green (for $\Phi > 0$) arrows for the available energy exchange. As a function of Φ: (b) available potential energy (continuous line) and background potential energy (dashed line), (c) normalized buoyancy flux $\overline{\phi}_y(\Phi)/\overline{\phi}_y(0)$, and (d) normalized buoyancy input $\overline{\phi}_{b2}(\Phi)/\overline{\phi}_{b2}(0)$. Instantaneous area-averaged kinetic energy vs time for (e) $\mathrm{Pr} = 4.3$ and (f) $\mathrm{Pr} = 0.1$ and three different inclination angles $\Phi = 0$ (black), $2\pi/9$ (purple), and $\pi/2$ (pink). (g) Mixing efficiency η as a function of Φ. E_p is the total potential energy. Symbols are for $\mathrm{Pr} = 0.1$ (circle) and $\mathrm{Pr} = 4.3$ (square). Colors are for $\mathrm{Ra} = 10^7$ (green) and $\mathrm{Ra} = 10^{10}$ (magenta).

fluxes and irreversible mixing contribute equally to heat transport, whereas when we increase the Φ, buoyancy fluxes reduce gradually, and irreversible mixing becomes more dominant. The heat transfer mechanism in inclined convection in any enclosure can be better understood with the help of the energy paths shown in Fig. 12(a).

VI. SUMMARY AND CONCLUSIONS

In this work, we have numerically investigated thermal convection in a quasi-two-dimensional circular enclosure in which the applied thermal gradient makes an inclination (Φ) with the gravity ($\mathbf{g}$). We varied the Rayleigh number (Ra) and the Prandtl number (Pr) in the ranges $10^7 \leqslant \mathrm{Ra} \leqslant 10^{10}$ and $0.1 \leqslant \mathrm{Pr} \leqslant 15$. The enclosure bottom is heated, and the top is cooled, similar to the classical RB convection, and the role played by Φ is studied in the range 0 to $\pi/2$. For $\Phi = 0$ (which resembles classical RB convection), we have observed a primary roll at the enclosure center (or bulk zone), supported by two secondary rolls near the conduction walls. Unlike the corner rolls in a square RB, the secondary rolls in a circular convection move around the enclosure periphery and induce massive thermal plumes and chaotic reversals. The growth of secondary rolls is prominent for $\mathrm{Pr} = 4.3$ and $10^7 \leqslant \mathrm{Ra} < 10^8$. Secondary rolls lose their identity at low Pr ($\leqslant 1$) and high Ra ($\geqslant 10^9$) due to large thermal diffusion and the strengthened primary roll. With an increase in Φ (> 0), thermal

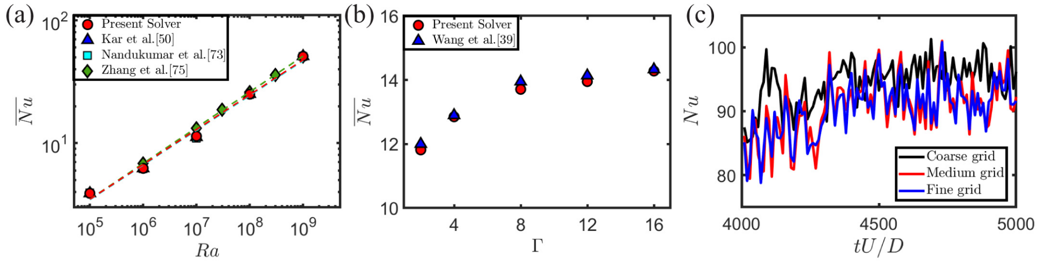

FIG. 13. (a) $\overline{\mathrm{Nu}}$ vs Ra for square RB convection at Pr = 1 are compared with Refs. [50,72,74]. (b) $\overline{\mathrm{Nu}}$ vs Γ for rectangular RB convection at $\mathrm{Ra} = 10^7$ and Pr = 0.71 are compared with Ref. [39]. (c) Instantaneous Nu for three grids: coarse (147 456 grids), medium (1 048 576 grids), and fine (7 463 824 grids).

plumes prefer to rise or fall along the enclosure periphery, and the primary roll maintains a nearly circular shape without any secondary rolls. For large Φ ($\geqslant \pi/6$), the primary roll destabilizes in the core bulk region in the form of a dipole, tripole, and multiroll structures, showing a small Reynolds number ($\mathrm{Re_{rms}}$), but with high Nusselt number (Nu). Stratified convection (with core bulk instabilities) develops for $\Phi \geqslant \pi/3$, with increased mixing and high bulk mean temperature. Using a transient scaling analysis, we have shown both Nu and Re based on velocity at the onset of the convection have a sine and cosine functional dependence on Φ, and our numerical results indeed capture such a trend. At small inclination angles, Nu increases linearly with Φ due to the strengthened primary roll; in contrast, at large angles, Nu decreases cubically due to the stratification effect. In the limited range $10^7 \leqslant \mathrm{Ra} \leqslant 10^{10}$, our results show $\mathrm{Nu} \propto \mathrm{Ra}^{\beta}$ and $\mathrm{Re} \propto \mathrm{Ra}^{\gamma}$, with the scaling exponents $\beta \approx 0.29$ and $\gamma \approx 0.56$ for $\Phi = 0$, and $\beta \approx 0.25$ and $\gamma \approx 0.3$ for $\Phi = \pi/2$. We have carried out the global energy budget and found that the buoyancy fluxes which convert the available potential energy into fluid convective motions decrease with an increase in Φ (thus Re decreases), but the irreversible fluid mixing, which homogenizes the thermal field, increases (thus Nu increases).

ACKNOWLEDGMENTS

Our sincere thanks to Prof. Jaywant H. Arakeri (IISc), Prof. Meheboob Alam (JNCASR), Prof. Chao Sun (Tsinghua University), and two anonymous referees for their inspiring discussions and suggestions on thermal convection. R.L. acknowledges research grants from the Board of Research and Nuclear Sciences (BRNS), the Mathematical Research Impact Centric Support (MATRICS) scheme, and the INSPIRE-DST scheme sponsored by the Government of India. We sincerely thank the National Supercomputing Mission–India and Param Shakti for providing the necessary computing resources.

APPENDIX: APPENDIX GRID CONVERGENCE DETAILS

Our solver is well tested for square and rectangular RB convection [see Figs. 13(a) and 13(b)]. We have also carried out a grid independence test [see Fig. 13(c)] for circular enclosure at $\mathrm{Ra} = 10^{10}$, Pr = 0.1, and Φ = 0 using three different grids: coarse (147 456 grids), medium (1 048 576 grids), and fine (7 463 824 grids). The time-averaged Nusselt numbers calculated based on medium and fine grids are within 0.08% error. The grid convergence index (GCI) calculated based on Richardson's extrapolation technique (see detailed procedure in our previous work [52]) is 1.16×10^{-3}. As the GCI is less than 1%, numerical solutions of the fine and medium grids are almost the same, and we have chosen a medium grid for our simulations.

Figure 14 shows the time-averaged energy in the first nine Fourier modes as a function of Φ for $\mathrm{Ra} = 10^7$ and Pr = 0.1, 4.3, and 15. In the case of Pr = 0.1, mode (1,1) is dominant and contains

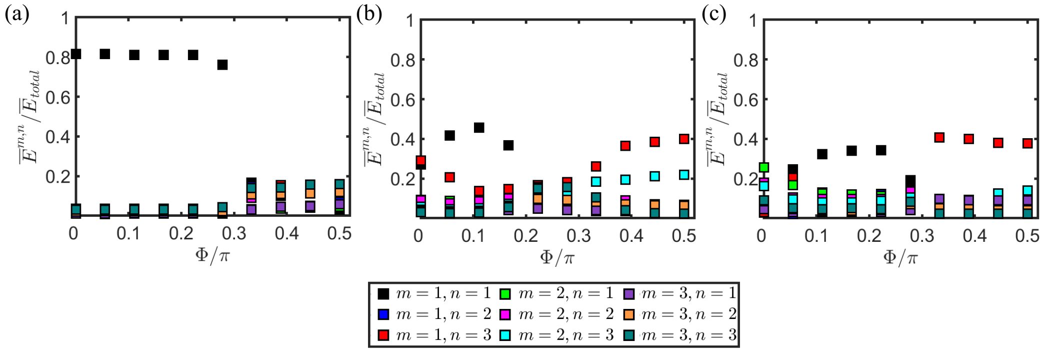

FIG. 14. Time-averaged energy contained in the first nine Fourier modes as a function of Φ for Ra $= 10^7$: (a) Pr $= 0.1$, (b) Pr $= 4.3$, and (c) Pr $= 15$.

more than 70% of the total energy until $\Phi \leqslant 5\pi/18$. Beyond $\Phi > 5\pi/18$, core bulk instabilities set in and six modes (1,2), (1,3), (2,2), (2,3), (3,2), and (3,3) together contain nearly 70% of the total energy. In the case of Pr $= 4.3$ and $\Phi = 0$, modes (1,1) and (1,3) are dominant; the dominance of mode (1,3) reduces and mode (1,1) increases gradually with increasing Φ until $\Phi \leqslant \pi/6$. In the range $\pi/6 < \Phi < \pi/3$, six modes (1,2), (1,3), (2,2), (2,3), (3,2), and (3,3) are equally dominant and after $\Phi \geqslant \pi/3$ the dominance of mode (1,3) gradually increases, which indicates flow stratification. In the case of Pr $= 15$ and $\Phi = 0$, modes (2,1), (2,2), and (2,3) are dominant, representing the chaotic state; dominance of mode (1,1) increases with Φ, until $\Phi < 5\pi/18$, and beyond $\Phi \geqslant \pi/3$ mode (1,3) becomes dominant.

Figure 15 shows $\overline{\text{Nu}}$ and $\overline{\text{Re}}_{\text{rms}}$ as functions of Φ. In the case of Pr $= 1$, Ra $= 10^7$, the increase rate of is higher for the small Φ where a single-roll flow structure is observed. Whereas for Pr $= 1$ and Ra $= 10^9$, $\overline{\text{Nu}}(\Phi)$ decreases for small Φ where a single-roll flow structure is observed. In the case of Pr $= 7$ and 15 initially for small Φ, $\overline{\text{Nu}}(\Phi)$ decreases, where the flow state changes from a chaotic to a circulation state with one primary and two secondary rolls; when secondary rolls get eliminated and a single-roll state starts appearing, $\overline{\text{Nu}}(\Phi)$ starts increasing and attains global maxima at $\Phi = 7\pi/18$. $\overline{\text{Re}}_{\text{rms}}(\Phi)$ continuously decreases with an increase in Φ except for the Ra $= 10^7$ and Pr $= 7$. In the case of Ra $= 10^7$ and Pr $= 7$, $\overline{\text{Re}}_{\text{rms}}(\Phi)$ increases with small Φ ($\leqslant \pi/18$) where Φ organizes the chaotic flow observed in the case of $\Phi = 0$ to the circulation state.

$$\frac{\partial (r u_r)}{\partial r} + \frac{\partial u_\theta}{\partial \theta} = 0, \tag{A1}$$

$$\frac{\partial u_r}{\partial t} + u_r \frac{\partial u_r}{\partial r} + \frac{u_\theta}{r}\frac{\partial u_r}{\partial \theta} - \frac{u_\theta^2}{r} = \frac{-1}{\rho_m}\frac{\partial P}{\partial r} + \nu\left[\frac{1}{r}\frac{\partial}{\partial r}\left(r\frac{\partial u_r}{\partial r}\right) + \frac{1}{r^2}\frac{\partial^2 u_r}{\partial \theta^2} - \frac{2}{r^2}\frac{\partial u_\theta}{\partial \theta} - \frac{u_r}{r^2}\right] + g_r[1 - \alpha(T - T_m)], \tag{A2}$$

$$\frac{\partial u_\theta}{\partial t} + u_r \frac{\partial u_\theta}{\partial r} + \frac{u_\theta}{r}\frac{\partial u_\theta}{\partial \theta} + \frac{u_r u_\theta}{r} = \frac{-1}{\rho_m}\left(\frac{1}{r}\right)\frac{\partial P}{\partial \theta} + \nu\left[\frac{1}{r}\frac{\partial}{\partial r}\left(r\frac{\partial u_\theta}{\partial r}\right) + \frac{1}{r^2}\frac{\partial^2 u_\theta}{\partial \theta^2} + \frac{2}{r^2}\frac{\partial u_r}{\partial \theta} - \frac{u_\theta}{r^2}\right] + g_\theta[1 - \alpha(T - T_m)], \tag{A3}$$

$$\frac{\partial T}{\partial t} + u_r \frac{\partial T}{\partial r} + \frac{u_\theta}{r}\frac{\partial T}{\partial \theta} = \kappa\left[\frac{1}{r}\frac{\partial}{\partial r}\left(r\frac{\partial T}{\partial r}\right) + \frac{1}{r^2}\frac{\partial^2 T}{\partial \theta^2}\right]. \tag{A4}$$

Equations (A1)–(A4) are the conservation of mass, momentum, and thermal energy equations in the cylindrical polar coordinates. Here cylindrical polar coordinates are (r, θ), $\mathbf{u} = (u_r, u_\theta)$ is the velocity field, P is the total pressure including a hydrostatic component, and $\mathbf{g} = (g_r, g_\theta)$ is the acceleration due to gravity.

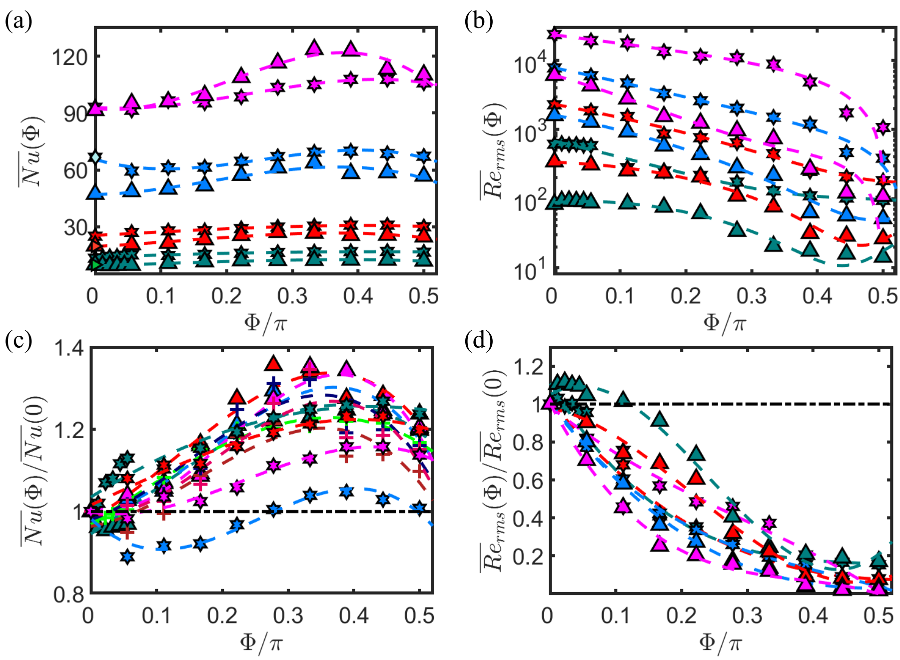

FIG. 15. As a function of Φ: (a) $\overline{\mathrm{Nu}}$, (b) $\overline{\mathrm{Re}}_{\mathrm{rms}}$, (c) $\overline{\mathrm{Nu}}(\Phi)/\overline{\mathrm{Nu}}(0)$, and (d) $\overline{\mathrm{Re}}_{\mathrm{rms}}(\Phi)/\overline{\mathrm{Re}}_{\mathrm{rms}}(0)$. Symbols are for $\mathrm{Pr} = 1$ (hexagram), $\mathrm{Pr} = 7$ (triangle), and $\mathrm{Pr} = 15$ (plus). Colors are for $\mathrm{Ra} = 10^7$ (green), $\mathrm{Ra} = 10^8$ (red), $\mathrm{Ra} = 10^9$ (blue), and $\mathrm{Ra} = 10^{10}$ (magenta). Dashed lines are for the best cubic fits. The black dash-dotted line at 1 in panels (c) and (d) is to guide the eye. Additional symbols: right-pointing triangle ($\mathrm{Pr} = 7$) [43] and diamond ($\mathrm{Pr} = 1$) [49] for $\overline{\mathrm{Nu}}$.

Figure 16(a) shows the ratio of simulation-based $\overline{\mathrm{Nu}}(\Phi)/\overline{\mathrm{Nu}}(0)$ and scaling-based $\mathrm{Nu}(\Phi)/\mathrm{Nu}(0)$ on the left y axis, and the ratio of simulation-based $\overline{\mathrm{Nu}}(\Phi)/\overline{\mathrm{Nu}}(\pi/2)$ and scaling-based $\mathrm{Nu}(\Phi)/\mathrm{Nu}(\pi/2)$ on the right y axis for $\mathrm{Pr} = 7$ and 15. The numerical simulations based on $\overline{\mathrm{Nu}}$ in the range $0 \leqslant \Phi < \pi/9$ follow the scaling law $\mathrm{Nu}(\Phi) \sim (\mathrm{Ra}\cos\Phi)^{1/3}$ while in the range $\pi/9 \leqslant \Phi \leqslant \pi/2$ they follow the scaling law $\mathrm{Nu}(\Phi) \sim (\mathrm{Ra}\sin\Phi)^{1/4}$. Figure 16(b) shows the ratio

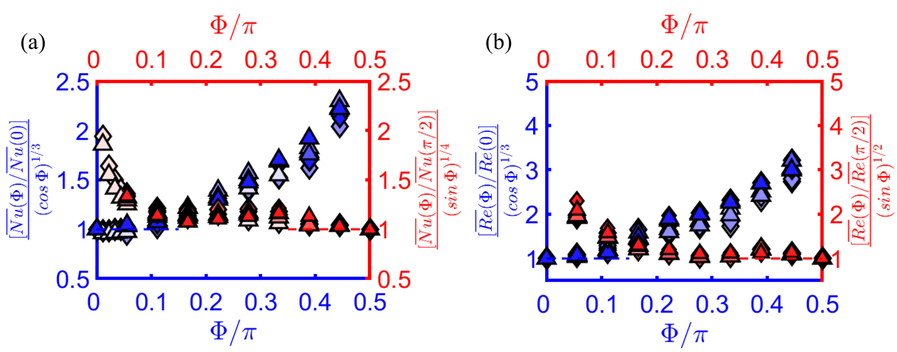

FIG. 16. As a function of Φ: (a) compensated $\overline{\mathrm{Nu}}$ and (b) compensated $\overline{\mathrm{Re}}$ based on time-averaged local velocity at the thermal boundary layer for $\mathrm{Pr} = 7$ (triangle) and $\mathrm{Pr} = 15$ (diamond). Left (blue) and right (red) y axes scale differently. Shades of blue and red vary from light to dark with increasing Ra for $\mathrm{Ra} = 10^7$, 10^8, 10^9, and 10^{10}. The dashed line at 1 is to guide the eye.

of simulation-based $\overline{\mathrm{Re}}$ (computed based on time-averaged local velocity at the thermal boundary layer) and scaling-based Re for Pr = 7 and 15.

---

[1] D. L. Hartmann, L. A. Moy, and Q. Fu, Tropical convection and the energy balance at the top of the atmosphere, J. Clim. **14**, 4495 (2001).
[2] S. Rahmstorf, The thermohaline ocean circulation: A system with dangerous thresholds? Clim. Change **46**, 247 (2000).
[3] J. Marshall and F. Schott, Open-ocean convection: Observations, theory, and models, Rev. Geophys. **37**, 1 (1999).
[4] P. Cardin and P. Olson, Chaotic thermal convection in a rapidly rotating spherical shell: Consequences for flow in the outer core, Phys. Earth Planet. Inter. **82**, 235 (1994).
[5] B. W. Atkinson and J. Wu Zhang, Mesoscale shallow convection in the atmosphere, Rev. Geophys. **34**, 403 (1996).
[6] J. Lin, T. Qian, P. Bechtold, G. Grell, G. J. Zhang, P. Zhu, S. R. Freitas, H. Barnes, and J. Han, Atmospheric convection, Atmos. Ocean **60**, 422 (2022).
[7] A. D. Brent, V. R. Voller, and K. J. Reid, Enthalpy-porosity technique for modeling convection-diffusion phase change: Application to the melting of a pure metal, Numer. Heat Transfer **13**, 297 (1988).
[8] G. R. Hunt and P. P. Linden, The fluid mechanics of natural ventilation—Displacement ventilation by buoyancy-driven flows assisted by wind, Build. Sci. **34**, 707 (1999).
[9] S. Kalogirou, Thermal performance, economic and environmental life cycle analysis of thermosiphon solar water heaters, Solar Energy **83**, 39 (2009).
[10] S. Kumar, Natural convective heat transfer in trapezoidal enclosure of box-type solar cooker, Renew. Energy **29**, 211 (2004).
[11] K. Hadad, A. Rahimian, and M. R. Nematollahi, Numerical study of single and two-phase models of water/Al_2O_3 nanofluid turbulent forced convection flow in VVER-1000 nuclear reactor, Ann. Nucl. Energy **60**, 287 (2013).
[12] H. M. S. Hussein, M. A. Mohamad, and A. S. El-Asfouri, Transient investigation of a thermosyphon flat-plate solar collector, Appl. Therm. Eng. **19**, 789 (1999).
[13] G. Ziskind, V. Dubovsky, and R. Letan, Ventilation by natural convection of a one-story building, Energy Build. **34**, 91 (2002).
[14] G. Ahlers, S. Grossmann, and D. Lohse, Heat transfer and large scale dynamics in turbulent Rayleigh-Bénard convection, Rev. Mod. Phys. **81**, 503 (2009).
[15] D. Lohse and K.-Q. Xia, Small-scale properties of turbulent Rayleigh-Bénard convection, Annu. Rev. Fluid Mech. **42**, 335 (2010).
[16] F. Chillà and J. Schumacher, New perspectives in turbulent Rayleigh-Bénard convection, Eur. Phys. J. E **35**, 58 (2012).
[17] K.-Q. Xia, Current trends and future directions in turbulent thermal convection, Theor. Appl. Mech. Lett. **3**, 052001 (2013).
[18] P. A. Davidson, *Turbulence: An Introduction for Scientists and Engineers* (Oxford University Press, New York, 2015).
[19] A. Bejan, *Convection Heat Transfer* (Wiley, New York, 2013).
[20] M. K. Verma, *Physics of Buoyant Flows* (World Scientific, Singapore, 2018).
[21] M. Lappa, *Thermal Convection: Patterns, Evolution and Stability* (Wiley, New York, 2009).
[22] N. Kousha, M. Hosseini, M. Aligoodarz, R. Pakrouh, and R. Bahrampoury, Effect of inclination angle on the performance of a shell and tube heat storage unit—An experimental study, Appl. Therm. Eng. **112**, 1497 (2017).
[23] K. A. Emanuel, J. D. Neelin, and C. S. Bretherton, On large-scale circulations in convecting atmospheres, Q. J. R. Meteorol. Soc. **120**, 1111 (1994).

[24] H. E. Huppert and J. S. Turner, On melting icebergs, Nature (London) **271**, 46 (1978).
[25] D. S. Russell-Head, The melting of free-drifting icebergs, Ann. Glaciol. **1**, 119 (1980).
[26] E. Rignot, S. Jacobs, J. Mouginot, and B. Scheuchl, Ice-shelf melting around Antarctica, Science **341**, 266 (2013).
[27] Z. Wang, L. Jiang, Y. Du, C. Sun, and E. Calzavarini, Ice front shaping by upward convective current, Phys. Rev. Fluids **6**, L091501 (2021).
[28] A. Bejan, Note on Gill's solution for free convection in a vertical enclosure, J. Fluid Mech. **90**, 561 (1979).
[29] A. Y. Vasil'ev, I. V. Kolesnichenko, A. D. Mamykin, P. G. Frick, R. I. Khalilov, S. A. Rogozhkin, and V. V. Pakholkov, Turbulent convective heat transfer in an inclined tube filled with sodium, Tech. Phys. **60**, 1305 (2015).
[30] R. Khalilov, I. Kolesnichenko, A. Pavlinov, A. Mamykin, A. Shestakov, and P. Frick, Thermal convection of liquid sodium in inclined cylinders, Phys. Rev. Fluids **3**, 043503 (2018).
[31] L. Zwirner and O. Shishkina, Confined inclined thermal convection in low-Prandtl-number fluids, J. Fluid Mech. **850**, 984 (2018).
[32] O. Shishkina and S. Horn, Thermal convection in inclined cylindrical containers, J. Fluid Mech. **790**, R3 (2016).
[33] F. Chillá, M. Rastello, S. Chaumat, and B. Castaing, Long relaxation times and tilt sensitivity in Rayleigh–Bénard turbulence, Eur. Phys. J. B **40**, 223 (2004).
[34] G. Ahlers, E. Brown, and A. Nikolaenko, The search for slow transients, and the effect of imperfect vertical alignment, in turbulent Rayleigh–Bénard convection, J. Fluid Mech. **557**, 347 (2006).
[35] L. Zhang, G.-Y. Ding, and K.-Q. Xia, On the effective horizontal buoyancy in turbulent thermal convection generated by cell tilting, J. Fluid Mech. **914**, A15 (2021).
[36] S.-X. Guo, S.-Q. Zhou, X.-R. Cen, L. Qu, Y.-Z. Lu, L. Sun, and X.-D. Shang, The effect of cell tilting on turbulent thermal convection in a rectangular cell, J. Fluid Mech. **762**, 273 (2015).
[37] L. Jiang, C. Sun, and E. Calzavarini, Robustness of heat transfer in confined inclined convection at high Prandtl number, Phys. Rev. E **99**, 013108 (2019).
[38] L. Zhang, J. Dong, and K.-Q. Xia, Exploring the plume and shear effects in turbulent Rayleigh-Bénard convection with effective horizontal buoyancy under streamwise and spanwise geometrical confinements, J. Fluid Mech. **940**, A37 (2022).
[39] Q. Wang, Z.-H. Wan, R. Yan, and D.-J. Sun, Multiple states and heat transfer in two-dimensional tilted convection with large aspect ratios, Phys. Rev. Fluids **3**, 113503 (2018).
[40] Q. Wang, S.-N. Xia, B.-F. Wang, D.-J. Sun, Q. Zhou, and Z.-H. Wan, Flow reversals in two-dimensional thermal convection in tilted cells, J. Fluid Mech. **849**, 355 (2018).
[41] H. Song, E. Villermaux, and P. Tong, Coherent oscillations of turbulent Rayleigh–Bénard convection in a thin vertical disk, Phys. Rev. Lett. **106**, 184504 (2011).
[42] Y. Wang, P.-Y. Lai, H. Song, and P. Tong, Mechanism of large-scale flow reversals in turbulent thermal convection, Sci. Adv. **4**, eaat7480 (2018).
[43] A. Xu, X. Chen, and H.-D. Xi, Tristable flow states and reversal of the large-scale circulation in two-dimensional circular convection cells, J. Fluid Mech. **910**, A33 (2021).
[44] N. Hasan, S. F. Anwer, and S. Sanghi, Natural convection in a bottom heated horizontal cylinder, Phys. Fluids **17**, 064105 (2005).
[45] H. Li, X. Ding, D. Jing, M. Xiong, and F. Meng, Experimental and numerical investigation of liquid-cooled heat sinks designed by topology optimization, Int. J. Therm. Sci. **146**, 106065 (2019).
[46] A. K. Poddar and N. K. Singh, Numerical study of liquid film formation around tubes of horizontal falling film evaporator, J. Appl. Fluid Mech. **14**, 1045 (2021).
[47] F. Aboosaidi, M. J. Warfield, and D. Choudhury, Numerical analysis of airflow in aircraft cabins, SAE Trans. **100**, 1294 (1991).
[48] Z. Anxionnaz, M. Cabassud, C. Gourdon, and P. Tochon, Heat exchanger/reactors (HEX reactors): Concepts, technologies: State-of-the-art, Chem. Eng. Process. **47**, 2029 (2008).

[49] W. Xu, Y. Wang, X. He, X. Wang, J. Schumacher, S.-D. Huang, and P. Tong, Mean velocity and temperature profiles in turbulent Rayleigh–Bénard convection at low Prandtl numbers, J. Fluid Mech. **918**, A1 (2021).
[50] P. K. Kar, Y. N. Kumar, P. K. Das, and R. Lakkaraju, Thermal convection in octagonal-shaped enclosures, Phys. Rev. Fluids **5**, 103501 (2020).
[51] P. K. Kar, U. Chetan, J. Mahato, T. L. Sahu, P. K. Das, and R. Lakkaraju, Heat flux enhancement by regular surface protrusion in partitioned thermal convection, Phys. Fluids **34**, 127105 (2022).
[52] P. K. Kar, U. Chetan, A. Kumar, P. K. Das, and R. Lakkaraju, Heat transport enhancement and flow transitions in partitioned thermal convection, Phys. Rev. Fluids **8**, 043501 (2023).
[53] O. Shishkina, R. J. A. M. Stevens, S. Grossmann, and D. Lohse, Boundary layer structure in turbulent thermal convection and its consequences for the required numerical resolution, New J. Phys. **12**, 075022 (2010).
[54] R. Lakkaraju, R. J. A. M. Stevens, R. Verzicco, S. Grossmann, A. Prosperetti, C. Sun, and D. Lohse, Spatial distribution of heat flux and fluctuations in turbulent Rayleigh–Bénard convection, Phys. Rev. E **86**, 056315 (2012).
[55] G. Grötzbach, Spatial resolution requirements for direct numerical simulation of the Rayleigh-Bénard convection, J. Comput. Phys. **49**, 241 (1983).
[56] See Supplemental Material at http://link.aps.org/supplemental/10.1103/PhysRevFluids.9.124305 for animations of the flow features in the circular enclosure.
[57] M. Chandra and M. K. Verma, Flow reversals in turbulent convection via vortex reconnections, Phys. Rev. Lett. **110**, 114503 (2013).
[58] K. L. Chong, S. Wagner, M. Kaczorowski, O. Shishkina, and K.-Q. Xia, Effect of Prandtl number on heat transport enhancement in Rayleigh-Bénard convection under geometrical confinement, Phys. Rev. Fluids **3**, 013501 (2018).
[59] K. Sugiyama, R. Ni, R. J. A. M. Stevens, T. S. Chan, S.-Q. Zhou, H.-D. Xi, C. Sun, S. Grossmann, K.-Q. Xia, and D. Lohse, Flow reversals in thermally driven turbulence, Phys. Rev. Lett. **105**, 034503 (2010).
[60] A. Castillo-Castellanos, A. Sergent, and M. Rossi, Reversal cycle in square Rayleigh–Bénard cells in turbulent regime, J. Fluid Mech. **808**, 614 (2016).
[61] E. Brown and G. Ahlers, Rotations and cessations of the large-scale circulation in turbulent Rayleigh-Bénard convection, J. Fluid Mech. **568**, 351 (2006).
[62] H.-D. Xi and K.-Q. Xia, Cessations and reversals of the large-scale circulation in turbulent thermal convection, Phys. Rev. E **75**, 066307 (2007).
[63] K. R. Sreenivasan, A. Bershadskii, and J. J. Niemela, Mean wind and its reversal in thermal convection, Phys. Rev. E **65**, 056306 (2002).
[64] F. F. Araujo, S. Grossmann, and D. Lohse, Wind reversals in turbulent Rayleigh-Bénard convection, Phys. Rev. Lett. **95**, 084502 (2005).
[65] S.-D. Huang and K.-Q. Xia, Effects of geometric confinement in quasi-2-D turbulent Rayleigh–Bénard convection, J. Fluid Mech. **794**, 639 (2016).
[66] Q. Wang, Z.-H. Wan, R. Yan, and D.-J. Sun, Flow organization and heat transfer in two-dimensional tilted convection with aspect ratio 0.5, Phys. Fluids **31**, 025102 (2019).
[67] E. P. van der Poel, R. J. A. M. Stevens, K. Sugiyama, and D. Lohse, Flow states in two-dimensional Rayleigh-Bénard convection as a function of aspect-ratio and Rayleigh number, Phys. Fluids **24**, 085104 (2012).
[68] Y. Zhang, Q. Zhou, and C. Sun, Statistics of kinetic and thermal energy dissipation rates in two-dimensional turbulent Rayleigh–Bénard convection, J. Fluid Mech. **814**, 165 (2017).
[69] J. Patterson and J. Imberger, Unsteady natural convection in a rectangular cavity, J. Fluid Mech. **100**, 65 (1980).
[70] B. Gayen, G. O. Hughes, and R. W. Griffiths, Completing the mechanical energy pathways in turbulent Rayleigh–Bénard convection, Phys. Rev. Lett. **111**, 124301 (2013).
[71] G. O. Hughes, B. Gayen, and R. W. Griffiths, Available potential energy in Rayleigh–Bénard convection, J. Fluid Mech. **729**, R3 (2013).

[72] Y. Nandukumar, S. Chakraborty, M. K. Verma, and R. Lakkaraju, On heat transport and energy partition in thermal convection with mixed boundary conditions, Phys. Fluids **31**, 066601 (2019).
[73] J. Marshall and R. A. Plumb, *Atmosphere, Ocean and Climate Dynamics: An Introductory Text* (Elsevier Academic Press, Cambridge, MA, 2008).
[74] Y. Zhang, Y.-X. Huang, N Jiang, Y.-L. Liu, Z.-M. Lu, X. Qiu, and Q. Zhou, Statistics of velocity and temperature fluctuations in two-dimensional Rayleigh–Bénard convection, Phys. Rev. E **96**, 023105 (2017).